ARMY RESEARCH LABORATORY

Experimental and Computational Studies of Oxidizer and Fuel Side Addition of Ethanol to Opposed Flow Air/Ethylene Flames

by Kevin L. McNesby, Andrzej W. Miziolek, Thuvan Nguyen, Frank C. Delucia, R. Reed Skaggs, and Thomas A. Litzinger

ARL-TR-3433 **February 2005**

NOTICES

Disclaimers

The findings in this report are not to be construed as an official Department of the Army position unless so designated by other authorized documents.

Citation of manufacturer's or trade names does not constitute an official endorsement or approval of the use thereof.

Destroy this report when it is no longer needed. Do not return it to the originator.

Army Research Laboratory
Aberdeen Proving Ground, MD 21005-5066

ARL-TR-3433 **February 2005**

Experimental and Computational Studies of Oxidizer and Fuel Side Addition of Ethanol to Opposed Flow Air/Ethylene Flames

Kevin L. McNesby, Andrzej W. Miziolek, Thuvan Nguyen, Frank C. Delucia, and R. Reed Skaggs
Weapons and Materials Research Directorate, ARL

Thomas A. Litzinger
Penn State University
State College, PA

REPORT DOCUMENTATION PAGE

Form Approved
OMB No. 0704-0188

1. REPORT DATE *(DD-MM-YYYY)*	2. REPORT TYPE	3. DATES COVERED (From - To)
February 2005	Final	September 2003–September 2004

4. TITLE AND SUBTITLE
Experimental and Computational Studies of Oxidizer and Fuel Side Addition of Ethanol to Opposed Flow Air/Ethylene Flames

5a. CONTRACT NUMBER

5b. GRANT NUMBER

5c. PROGRAM ELEMENT NUMBER

6. AUTHOR(S)
Kevin L. McNesby, Andrzej W. Miziolek, Thuvan Nguyen,
Frank C. Delucia, R. Reed Skaggs, and Thomas A. Litzinger*

5d. PROJECT NUMBER
62268.H8011

5e. TASK NUMBER

5f. WORK UNIT NUMBER

7. PERFORMING ORGANIZATION NAME(S) AND ADDRESS(ES)
U.S. Army Research Laboratory
ATTN: AMSRD-ARL-WM-BD
Aberdeen Proving Ground, MD 21005-5066

8. PERFORMING ORGANIZATION REPORT NUMBER
ARL-TR-3433

9. SPONSORING/MONITORING AGENCY NAME(S) AND ADDRESS(ES)

10. SPONSOR/MONITOR'S ACRONYM(S)

11. SPONSOR/MONITOR'S REPORT NUMBER(S)

12. DISTRIBUTION/AVAILABILITY STATEMENT
Approved for public release; distribution is unlimited.

13. SUPPLEMENTARY NOTES
*Penn State University, State College, PA

14. ABSTRACT
Results of computations based upon a detailed chemical kinetic combustion mechanism and results of experiments are compared to understand the influence of ethanol vapor addition upon soot formation and OH radical concentration in opposed flow ethylene/air diffusion flames. For this work, ethanol vapor was added to either the fuel or the oxidizer gases. Experiment and calculations are in qualitative agreement, and both show differing concentrations of soot, soot precursors, and OH depending on whether the ethanol is added to the fuel or oxidizer gases. An explanation for the observed differences for oxidizer or fuel side ethanol addition to opposed flow ethylene/air diffusion flames is proposed, based upon an analysis of the chemical kinetic mechanism used in the computations.

15. SUBJECT TERMS
soot formation, opposed flow flames, ethylene flames, ethanol, PLIF

16. SECURITY CLASSIFICATION OF:			17. LIMITATION OF ABSTRACT	18. NUMBER OF PAGES	19a. NAME OF RESPONSIBLE PERSON
a. REPORT	b. ABSTRACT	c. THIS PAGE			Kevin L. McNesby
UNCLASSIFIED	UNCLASSIFIED	UNCLASSIFIED	UL	50	19b. TELEPHONE NUMBER (*Include area code*) 410-306-0715

Standard Form 298 (Rev. 8/98)
Prescribed by ANSI Std. Z39.18

Contents

List of Figures

List of Tables

Acknowledgments

Funding support for this work was provided by the U.S. DOD Strategic Environmental Research and Development Program. The authors would like to thank Michael Frenklach and Charles Westbrook for much of the chemical mechanism used in the calculations. Also, the authors would like to thank Sukh Sidhu, Med Colket, Valeri Babushok, and William Anderson for helpful discussions.

1. Introduction

It is estimated that U.S. military aircraft emit about 600,000 kg of particulate matter into the atmosphere each year. Most of this particulate matter is in the form of soot particles with diameters <2.5 μm (PM2.5) (*1*). In addition to shortening engine life and limiting the time between engine servicing, there is a growing body of evidence that shows these small particles cause both health and environmental problems (*2–4*).

As part of a Strategic Environmental Research and Development Program effort investigating superefficient (ppm level) fuel additives for soot reduction in turbine engines (*5*), fundamental studies of the effects of additives on soot formation and oxidation in different types of burners and combustors are underway at several laboratories using a wide range of diagnostic methods. Part of the rationale of this program is to use different types of burners and combustors (diffusion, premixed, well-stirred reactors, etc.) to approximate the different stages of fuel combustion that occur in a turbine engine. For the initial series of experiments for this program, ethylene was chosen as the fuel because it has been used in past studies of soot formation processes in a wide range of burners (*6*). The part of the effort conducted at the U.S. Army Research Laboratory uses an opposed flow burner to investigate ethylene/air combustion.

Soot reducing additives studied in the past largely fall into two categories: metal based additives and oxygenated compounds (*6*). Although often very effective at soot reduction, the investigation of metal additives was ruled out due to concerns about adverse health and environmental impact as well as incompatibility with gas turbines. Thus, the use of oxygenated compounds (that are drawing increasing attention for use in diesel engines) was selected (*7*). It is worthwhile to note that oxygenated compounds are not seen as an ultimate solution to the particulate emission problem for gas turbine engines, because for noticeable effect they must be added at high concentrations (percent levels) to the fuel (*7*) , making them impractical. However, they do provide a good benchmark for the standardization tests. After considering the available data in the literature and compatibility with tests using ethylene, ethanol was selected as the initial additive compound to be studied (*8*, *9*). The choice of ethanol and ethylene also allowed chemical mechanisms from the literature to be used in modeling of the results (*10*).

2. Background

The separation of the regions of highest particulate and aromatic concentrations (sooting region) and the main combustion (flame radical production) region in opposed flow flames has been reported in the literature (*11*). We are aware of only one investigator using simultaneous planar laser induced fluorescence (PLIF) and light scattering measurements in sooting opposed flow

diffusion flames (*12*). Simultaneous measurement has been reported in the literature for co-flowing diffusion flames (*13*). For sooting opposed flow flames, peak soot concentration typically occurs near the stagnation plane, in fuel rich regions at temperatures slightly lower than peak combustion temperatures (*14*). For opposed flow diffusion flames in which the stagnation plane is fuel rich (e.g., the flame reported here), the flame occurs at the location where fuel and oxidizer are close to stoichiometric combustion proportions. This occurs on the oxidizer side of the stagnation plane (see figure 1), and the stoichiometric mixture is achieved by fuel gases diffusing upstream into the oxidizer flow. For the flames used here (ethylene/air) the overall chemical reaction (assuming air to be 20% oxygen) is

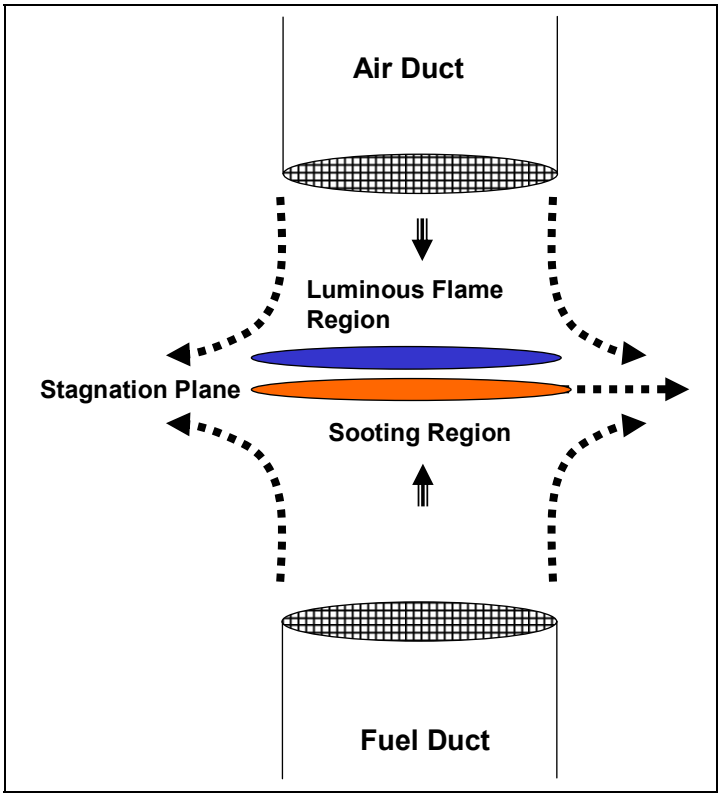

Figure 1. A schematic of the opposed flow burner and flame.

$$C_2H_4 + 3O_2 + 12\ N_2 \rightarrow 2CO_2 + 2H_2O + 12\ N_2\,. \qquad (1)$$

Reaction 1 shows that for fuel (C_2H_4) and oxidizer (air) flow rates that are approximately equal, in an opposed flow burner (our conditions), assuming gases with similar momenta (our conditions), the gas mixture at the stagnation plane will be fuel rich (*14*). The stagnation plane is conceptually shown in figure 1. The stagnation plane is typically described as the location between the gas and oxidizer ducts where the axial gas velocity goes to zero. For these experiments, the stagnation plane location was not measured, but was estimated by calculation.

For opposed flow flames that exhibit similar separations of sooting (particle laden) and flame (i.e., luminous) regions (e.g., ethylene/air, propane/air, heptane/air [in the authors' experience]), the effect of additives upon flame structure, radical formation, and extinction strain rate may be different depending on whether the additive is added to the fuel or oxidizer stream. As an example, when iron pentacarbonyl ($Fe[CO]_5$) is added to the air stream of many opposed flow hydrocarbon/air flame systems, it is among the most efficient flame inhibitors known. For fuel stream addition, the effect, on a molar basis, is much less pronounced (*15*).

The analysis of the experimental work described here attempts to understand the effect of fuel or air side addition of ethanol upon soot formation and OH radical concentrations in opposed flow ethylene/air flames. The approach focuses on a comparison of experimental results with results of flame modeling calculations incorporating the well-characterized C_2 combustion mechanism of Frenklach et al. (*10*). This mechanism was developed for premixed flame systems; we have used it here without modification. It may be worth noting that the activation energies for some reactions in the mechanism may exhibit a pressure dependence in ethylene/air counterflow flames (*16*). As previously mentioned, the experiments take advantage of the spatial separation between regions of peak soot (particles) and OH concentrations in the opposed flow ethylene/air flames. This spatial separation allows a single laser pulse, tuned to resonance with an OH absorption, to be used to simultaneously measure OH laser induced fluorescence (LIF) and light scattering (Mie + Rayleigh) by soot particles.

3. Experimental Conditions

The opposed flow burner is constructed of 304 stainless steel and is based upon the design of Lentati and Chelliah (*17*). Fuel (ethylene) and oxidizer (air) ducts are 15 mm in diameter and are separated by 10 mm. Flow rates for the experiments reported here were 4.6-L/m ethylene and 6.2-L/m air. These values were chosen because they gave the most stable flame. Ethanol vapor was added to fuel or oxidizer gases using an injection pump (Isco). The ethanol was injected as a liquid at room temperature into the fuel or oxidizer gas lines ~2 m upstream from the gas entrance into the burner assembly and was assumed to vaporize completely. Ethanol addition was up to 0.08 mole fraction (8%) in the fuel or oxidizer gas stream. It should be noted that this level (8%) of addition to the oxidizer stream makes the "oxidizer" a rich fuel/air mixture. The change in flame behavior as the oxidizer gas stream is transitioned to a fuel/air mixture is treated in detail in what follows. A shroud gas (nitrogen) surrounded both fuel and oxidizer ducts within the burner assembly to minimize entrainment of room air into the flame. The burner was enclosed in a chamber that was capable of being evacuated. However, for these experiments the access ports of the chamber were left open and so all experiments were run at atmospheric pressure. A schematic of the experimental apparatus is shown in figure 2.

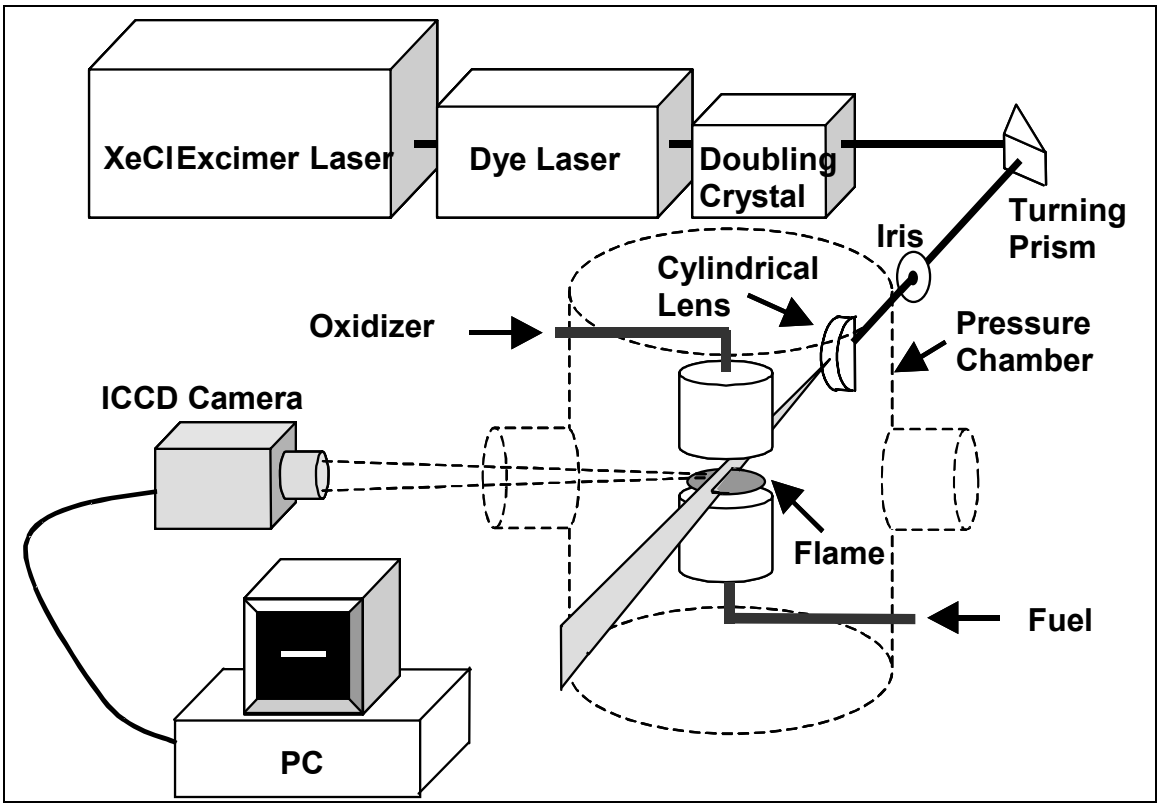

Figure 2. A schematic of the experimental apparatus.

The experimental procedure was as follows. A flame source was placed between the burner ducts and gas flow was then commenced, with the opposed flow flame igniting immediately. The nitrogen shroud gas flow (5 L/m total) was initiated and the flame was allowed to stabilize for 5 min. For experiments using fuel or oxidizer additive, a valve on the injection pump was opened and flow of ethanol into the air or ethylene streams was begun. After ~1 min of flow of ethanol, a sheet of pulsed laser radiation (typically 0.5 mJ/pulse, ~20 ns duration, formed using a double apertured, half cylindrical lens) near a wavelength of 281 nm (Lambda Physik Excimer/Scanmate system: Coumarin 153 dye: Fundamental @ 560 nm, 2x frequency to 281 nm; Pump $A^2\Sigma^+$ (v = 1) ←$X^2\Pi$ (v = 0), detect [(0,0), (1,1)] around 310 nm) was passed through the flame region. A gated, unfiltered, intensified CCD camera (Roper Scientific, 256 × 1024 pixels), equipped with a Nikor 1:4.5 UV lens, was used to measure laser scatter during and immediately following the laser pulse (camera gate width = 80 ns). The images produced by 100 laser pulses were averaged in the camera memory. From this average image, the maximum value at a given pixel location along the centerline between the fuel and oxygen ducts was selected in the sooting and combustion regions of the flame (see figure 3). A background value at that pixel location, measured prior to the flame initiation (also 100 averaged images), was subtracted from this value. This background corrected pixel value became the data point representing peak particle or OH concentration. Following data collection, the injection pump valve was closed, the pump flow parameters were reset, and the process repeated. Planar laser

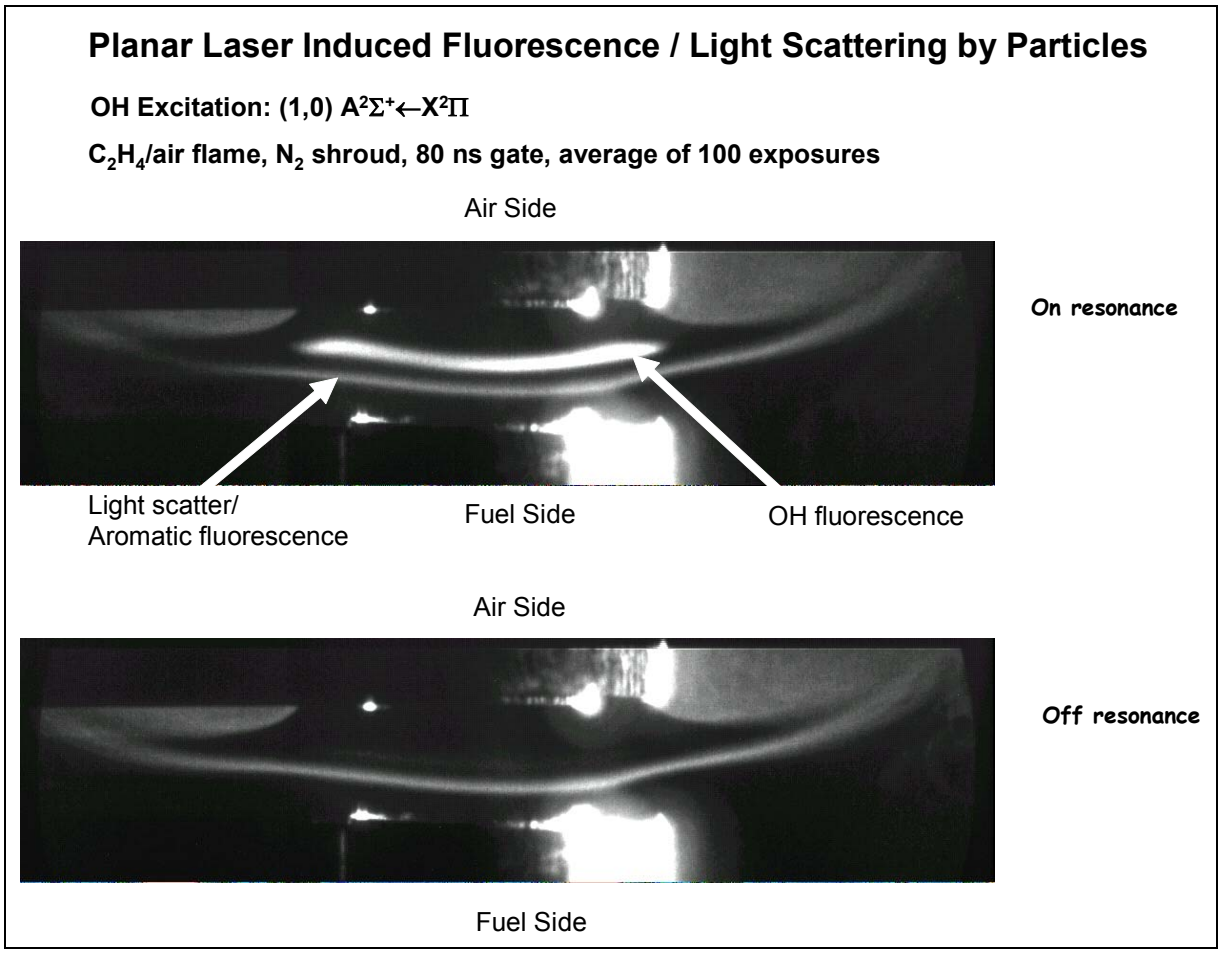

Figure 3. Upper: simultaneous image of OH PLIF and light scattering by soot particles. Lower: same image, but with the laser tuned off of resonance with the OH absorption.

induced fluorescence and light scatter measurements at the beginning and end of each run series were performed to check that the flame returned to normal after the ethanol flow was stopped. Laser power was measured before and after each experimental run and typically varied by <2%. Other than subtraction of background, no corrections were made for changes in laser power or variations in spatial intensity, and no other specific dark field pixel corrections were made, although previous measurements of the CCD dark field (camera blocked) showed pixel to pixel output to vary by <2%.

The region of the flame referred to as the sooting region (and other flame regions) may contain particles and poly-aromatic hydrocarbons (PAH). These PAH are known to fluoresce when exposed to ultraviolet radiation (*18*). For the experiments reported here, we are assuming that the bulk of the signal observed in the sooting region is from scattered laser radiation (*19*). To evaluate the part of the observed image in the sooting region due to light scatter, we divided the theoretical treatment of the scattering process into an extinction part and a Mie theory part (*20–22*).

The intensity of scattered laser light (assuming unit incident intensity and zero absorption) by particles in the flame may be approximated by Bouguer's Law:

$$I = \exp(-3Q_e m_p L / 2\rho d). \quad (2)$$

Here, I is the intensity of the scattered light, Q_e is the soot extinction coefficient, m_p is the weight of soot particles per unit volume, L is the pathlength, and ρ and d are the density and diameter of the average soot particle. This equation predicts that as soot particle size (d) decreases for a fixed soot mass per unit volume, scattering intensity increases.

According to Mie's solution of Maxwell's equations in spherical coordinates for an electromagnetic wave incident on a sphere (*22*), the angular distribution of intensity and degree of polarization of the light scattered by a collection of particles is related to both the size and index of refraction of the particles. The general solution describing scattering of monochromatic light by a single particle of any size may be described by

$$I_\theta = \lambda^2/(8R^2\pi^2)[i_1(\theta) + i_2(\theta)]. \quad (3)$$

Here, I_θ is the light intensity scattered at angle θ , λ is the wavelength of the incident radiation, R is the distance from the particle to the point of observation, and $i_1(\theta)$ and $i_2(\theta)$ are angular distribution intensity functions that are dependent upon the intensities of the two plane polarized components of the scattered monochromatic incident light.

Application of Mie's solutions for light scattering by particles is usually simplified by considering the limiting cases where the particle diameter is much smaller than the wavelength of light (Rayleigh scattering, λ^{-4} intensity dependence), near the wavelength of light (Mie scattering), or much greater than the wavelength of light (diffractive optics). For light scattering by nascent soot particles in opposed flow flames (soot particle sizes of tens to hundreds of nanometers), the scattering is typically categorized as having characteristics of Rayleigh and Mie scattering. For observation at 90° to the incident beam, scattering in both Rayleigh and Mie regions is predicted to be perpendicularly polarized and non-zero.

So, for measurement of scattering intensity perpendicular to the incident laser beam, by a cloud of spherical particles with fixed size distribution, in the limit of $(3Q_e m_p L / 2\rho d) \ll 1$, the scattering intensity should be approximately proportional to m_p, and hence to soot volume fraction.

Figure 3 shows images of simultaneous light scattering and OH LIF taken perpendicular to the plane of the laser sheet. In this figure, the regions of maximum particle concentration and OH formation are seen to be well separated. Also shown in the figure is an image taken of the same flame with the laser tuned off of resonance with the OH absorption transition ([1,0] $A^2S \leftarrow X^2P$). Calculations used the OPPDIF flow code, based upon the Chemkin database, marketed by Reaction Design, Inc. The chemical mechanism input to the OPPDIF flow code used the Frenklach mechanism (*10*) for ethane combustion, modified by one of us (Litzinger) to include ethanol addition. The final chemical mechanism incorporates 156 species and contains 659 reactions. Input conditions for the calculations assumed initial gas temperatures at 300 K, 1 atmosphere total pressure, duct separation of 1 cm, and initial fuel and oxidizer gas stream velocities of 41 and 55 cm/s, respectively. For the burner system used in the experiments, the fuel velocity was ~41 cm/s, and the oxidizer velocity was ~55 cm/s. Duct separation was 1 cm. Each calculation required ~100 min to reach convergence on a Pentium 4-based desktop computer. The results of the Chemkin calculations predict flow parameters (gas velocity, strain, etc.), temperature, and species profiles as a function of distance from the fuel duct. The Frenklach mechanism allows prediction of species profiles for aromatic rings up to A4 ($C_{16}H_{10}$).

Two approaches were used for the calculations. In the first approach, the initial conditions input to the program specified a 60-point space grid between the burner ducts, with grid spacings becoming smaller near the combustion region. As the calculation proceeds, the program regrids to finer increments. When this initial grid was used, calculations often had difficulty converging, or took several hours to converge. The second approach used a five point, evenly spaced grid as the initial condition. The program was then allowed to regrid as the calculation proceeded. In every case for which convergence was achieved, although final results for the two approaches agreed, the second approach converged faster. Convergence criteria used for Newton iteration and for time stepping were the program default values, with the exception of the cases of 5% to 8% ethanol added to the air stream. To achieve convergence for these cases, it was necessary to relax the convergence criteria by a factor of 100. This reduction was achieved by relaxing the default values for the absolute and relative convergence criteria for Newton iteration from default values of 10^{-9} and 10^{-4}, respectively, to 10^{-7} and 10^{-2}. The absolute and relative convergence criteria for time stepping were also relaxed from default values of 10^{-9} and 10^{-4}, respectively, to 10^{-7} and 10^{-2}. The final grid for these cases contained ~2/3 the number of grid points as for the other calculations (from 97 to 65). The calculated results for all cases are included for completeness.

4. Results and Discussion

4.1 Neat Ethylene/Air Opposed Flow Flames

Figure 4 shows a graph of calculated mole fraction profiles vs. distance from the fuel duct for OH, C_2H_2, C_3H_3, A1 (benzene, C_6H_6), and A4 (pyrene, $C_{16}H_{10}$) for a neat ethylene/air opposed flow flame. Overlaid onto figure 4 are values of pixel intensity along the centerline between the burner ducts, measured using the light scattering/PLIF technique, for the same flame. The calculation is in reasonable agreement with observation. The calculation predicts the separation of regions of maximum soot concentration (assuming A1 through A4 to be soot precursors in fuel rich environments [*23–25*]), and OH. The experimental data in this figure have been background corrected by subtracting the pixel dark current. To compare the data, the spatial location of the peak from OH fluorescence (relative to the fuel duct) measured in the flame was matched to the spatial location of the peak from OH predicted by the calculation. The measured light scatter from particles in the flame (and also possible broad band fluorescence from aromatics) is slightly closer to the fuel duct than the location of peak A1 and A4 concentrations predicted by the calculation. Because the soot particles in the flame are likely larger than A4, thermophoretic forces (*26*) may be driving the larger particles towards cooler regions of the flame. Also shown in figure 4 (dashed line) is an estimation of the location of the stagnation plane, based upon the calculations. We have given the stagnation plane a finite width defined by the point where the axial gas velocity goes to zero (~0.375 cm from the fuel duct) and the point where the radial gas velocity is at a maximum (~0.428 cm from the fuel duct). The initial fuel and oxidizer gas stream velocities (for experiment and calculation) were 41 and 55 cm/s, respectively.

To understand how adding ethanol vapor to the fuel or oxidizer gases will affect the concentrations of OH and particles, we begin by identifying the main chemical reactions in our mechanism responsible for the conversion of ethylene to A1 (benzene) in neat opposed flow flames. The approach we used takes advantage of the post processor utility available in Chemkin that allows calculation of the rates of production and destruction of each species in the mechanism by each reaction involving that species. Figure 5 shows the rate of production of A1 vs. distance from the fuel duct for the top four contributing reactions in the mechanism (out of 15 reactions in the mechanism involving A1). To assign a percent contribution to A1 formation to each reaction, the area under the curve (divided by the local gas velocity) for each reaction was integrated, and this area per reaction compared to the area for the total rate of production for A1 (not shown in figure 5). According to this method, for A1 production in our neat ethylene/air opposed flow flame, the contribution of these 4 reactions is

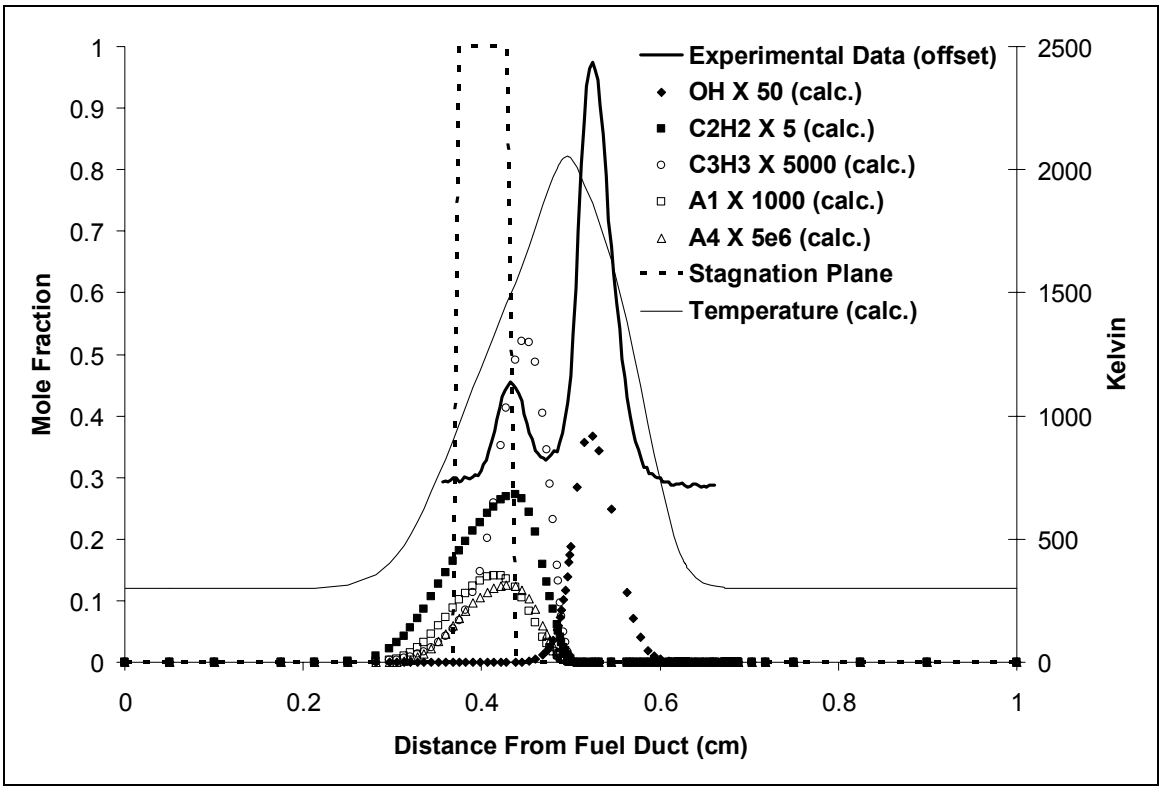

Figure 4. Results of calculations showing temperature profile and separation of soot forming and flame radical regions for an undoped ethylene/air opposed flow flame, with overlay of measured centerline pixel intensities for similar flame. Also shown is estimated position of stagnation plane.

$C_3H_3 + C_3H_3 \rightarrow A1$ 73% (4)

n-C4H5 + C2H2 → A1 + H 12% (5)

l-C6H6 + H → A1 + H 8% (6)

n-C6H7 → A1 + H 6% (7)

It is worth noting that l-C_6H_6 and n-C6H7 are dependent upon reactions of n-C_4H_5 with acetylene. For radical species that are formed in one part(s) of the flame, and consumed in other parts of the flame, it is necessary to modify this approach by limiting the regions of integration.

This approach was used in the neat opposed flow ethylene/air flame to follow carbon as it passed from ethylene to A1. When the conversion from one species to another in the flame was near quantitative (such as the initial decomposition step of C_2H_4 to C_2H_3), tracing the reaction was straightforward. When the main path to A1 production was less than quantitative for destruction of a certain species (such as CH_2 conversion to C_3H_3), it was necessary to examine the contribution of all reactions to production and destruction rates for species participating in a given reaction. Using this method, the path to A1 from ethylene begins with the conversion of

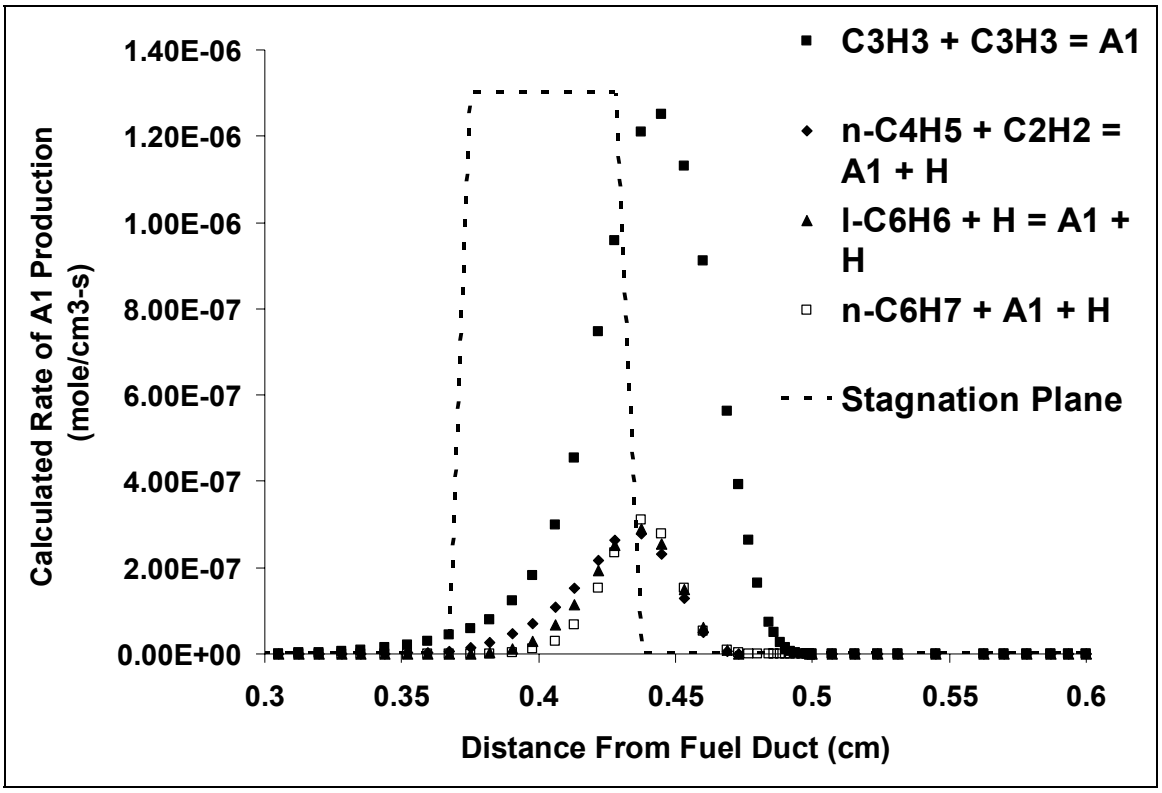

Figure 5. The calculated rates of production of A1 vs. distance from the fuel duct for the top four contributing reactions in the mechanism (out of 15 reactions in the mechanism involving A1). Calculation is for the neat ethylene/air opposed flow diffusion flame. Also shown is estimated position of stagnation plane.

C_2H_4 to C_2H_3 (99%, via H and OH), followed by conversion of C_2H_3 to acetylene (C_2H_2) (90%). The formation of this acetylene "bath" is important to the chemistry of soot formation. However, as the initial ethylene/air mixture is fuel rich, ~44% of the acetylene formed in this step remains unreacted. The mechanism contains 77 reactions in which acetylene is a participant. Approximately 34% of the acetylene is converted to methylene (CH_2) and singlet methylene (CH_2^*), of which ~4% is converted to propargyl (C_3H_3), of which ~6% is converted to A1. Although propargyl is the main source of A1 formation, only a small fraction of propargyl reacts directly to form A1.

Table 1 shows the stepwise conversion of ethylene to A1 predicted by the calculation for this flame system, lists the reactions important for A1 formation, and some of the important competing reactions (where applicable) for steps leading to A1 production. Species in bold face in the reaction list on the right side of table 1 are the species for which the rate of destruction (ROD) listed applies. Also shown is the temperature at which maximum ROD and rates of production (ROP) for several species occur.

Table 1. Reaction path of ethylene to A1 for neat ethylene/air opposed flow diffusion flames. Important reactions contributing to each species concentration are shown to the right. Percentage value in parenthesis refers to the amount of species in bold consumed or produced by that reaction.

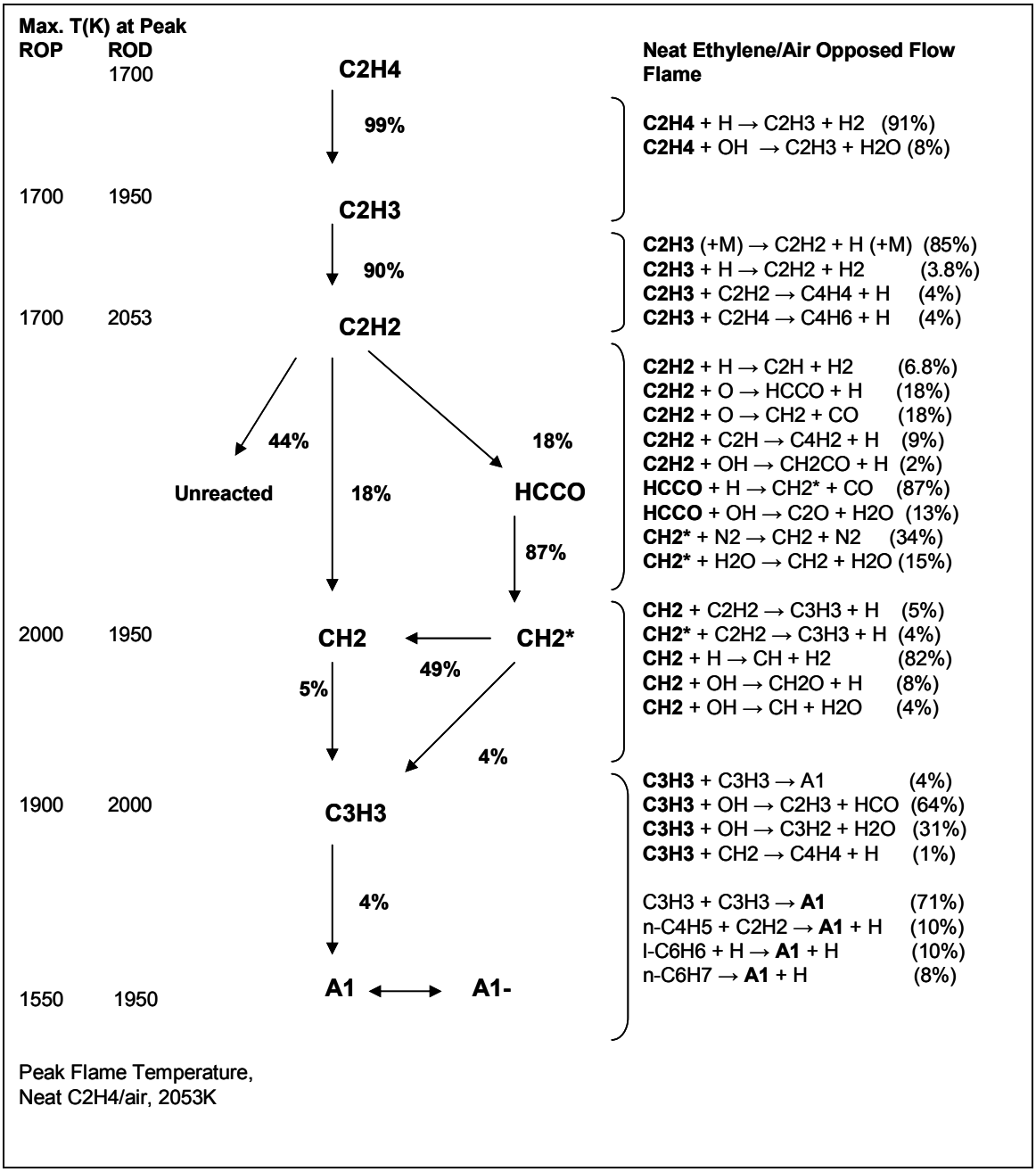

4.2 Oxidizer Side Addition of Ethanol

In experiments and calculations, oxidizer side addition of ethanol vapor reduces soot and soot precursors. A graph of experimental measurements of peak light scatter and OH fluorescence and predictions of species maximum mole fraction based upon calculations, for oxidizer side addition of ethanol, is shown in figure 6. The error in the measured scattered laser intensity and OH fluorescence is estimated to be ~5%, based upon pixel to pixel noise in the individual images. Overall, the change with increasing ethanol addition of calculated peak mole fractions for the species C_2H_2, A1 and A4 is in reasonable agreement with peak experimental values (measured along the centerline between burner ducts) of light scatter, while the change with increasing ethanol addition of the calculated peak mole fraction of OH is in average agreement with peak measured values of OH fluorescence, with calculation and experiment predicting a small decrease in peak OH concentration with ethanol addition. The slight increase in light scattering when ethanol vapor addition increases above 5% may be due to the transition from a diffusion flame to a partially premixed diffusion flame, and the onset of a secondary flame as the oxidizer mixture approaches premixed stoichiometry.

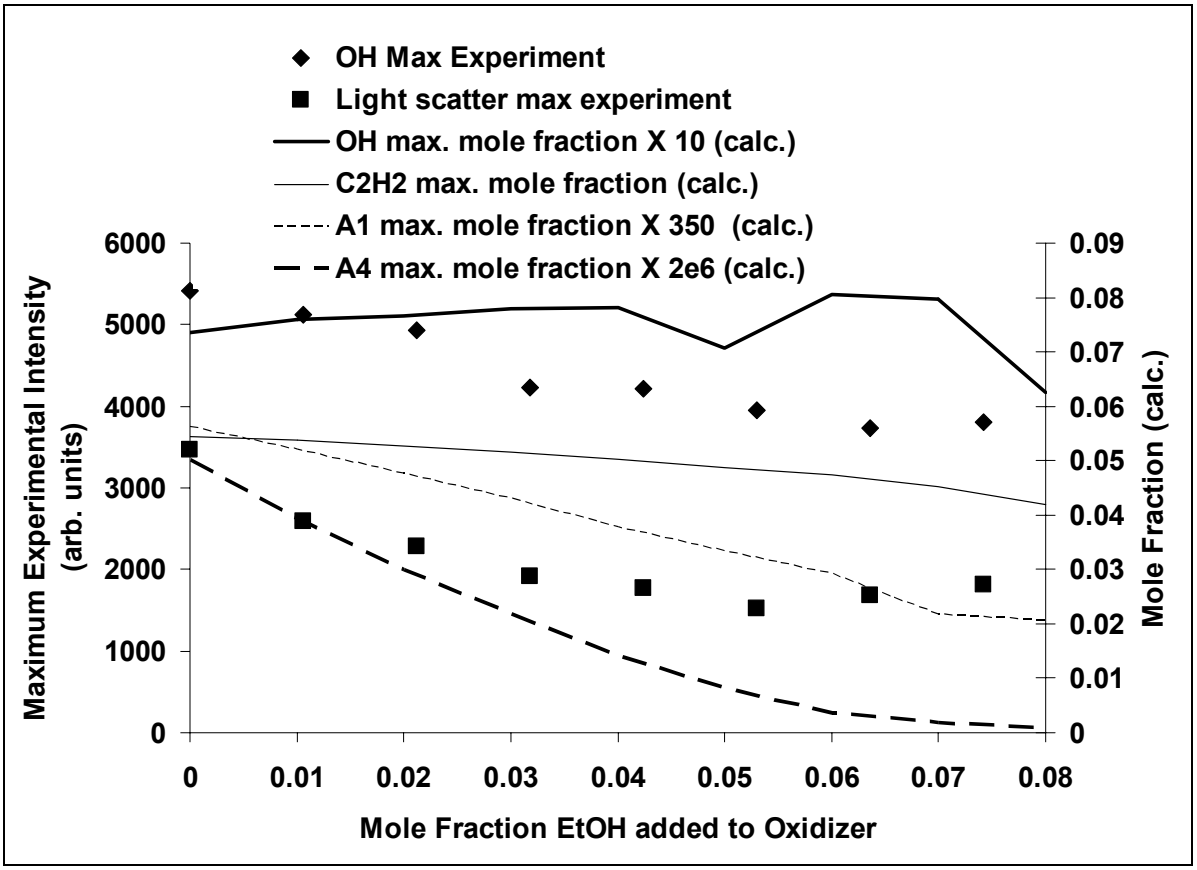

Figure 6. Graph of experimental measurements and predictions based upon calculations for OH, soot, and soot precursors, for air side addition of ethanol.

These results (decrease in soot, negligible change in peak OH concentration) at first seem contradictory. Soot reduction by addition of an oxygenated species is generally interpreted to be caused by an increase in local OH radical (*27*) concentration, leading to increased soot oxidation:

$$C_xH_y \text{ (soot)} + OH \rightarrow CO_2 + H_2O \ . \qquad (8)$$

However, examination of the individual experimental images (figure 7) shows that as ethanol is added to the oxidizer (air) stream, the width of the OH region increases. We believe that the broadening of the OH region for this flame is the key to understanding the decrease in measured light scattering by particles. Figures 8 and 9 show calculated temperature and OH mole fraction as a function of distance from the fuel duct. These figures show that the calculation predicts broadening of the OH and high temperature flame regions with increasing oxidizer side ethanol addition. Figure 10 shows the calculated ROD of 4% ethanol vapor added to the oxidizer side of the opposed flow flame, overlaid with the calculated temperature profile for this flame and for the neat flame. The region of ethanol destruction is shown to coincide in location with the onset of the broadened region of high temperature in the flame to which ethanol has been added. We believe this broadened region of high temperature is indicative of a secondary flame zone as the oxidizer gas gradually changes to a fuel/air gas mixture.

Qualitatively, addition of ethanol vapor to the air stream causes the flame to change from a diffusion flame towards a partially premixed diffusion flame. The broadening of the OH region and of the temperature profile moves the flame region (i.e., region of appreciable flame radical concentration and high temperature) closer to the stagnation plane, and therefore closer to the region of maximum soot concentration, thereby increasing the rate of soot oxidation (see figures 8 and 9). Introduction of ethanol to the air stream moves the flame from a soot formation type towards a soot formation/oxidation type, in which soot particles must travel a shorter distance into the oxidation region (*14*). As more ethanol vapor is added to the air stream, the flame begins transition to a multiple flame structure due to partial premixing as has been studied with other fuel-rich-oxidizer premixed flames (*28*).

To explore further the mechanism of particle reduction in these flames, table 2 shows the stepwise reactions of ethanol added to the oxidizer stream predicted by the calculation for this flame system. This table shows the reaction of ethanol and air in the premixed region of the diffusion flame. This region is the region between the oxidizer duct and the diffusion flame zone, when there is ethanol vapor mixed in with the oxidizer gas. As in table 1, species in bold face in the reaction list on the right side of table 2 are the species for which the ROD listed apply. Also shown is the temperature at which maximum ROD and ROP for several species occur. Table 2 shows that in the lean premixed flame region, the ethanol vapor is converted by a series of oxidation reactions (mainly involving H atom abstraction) to eventually yield OH and CO, prior to reaching the main combustion region of the diffusion flame (see figure 10).

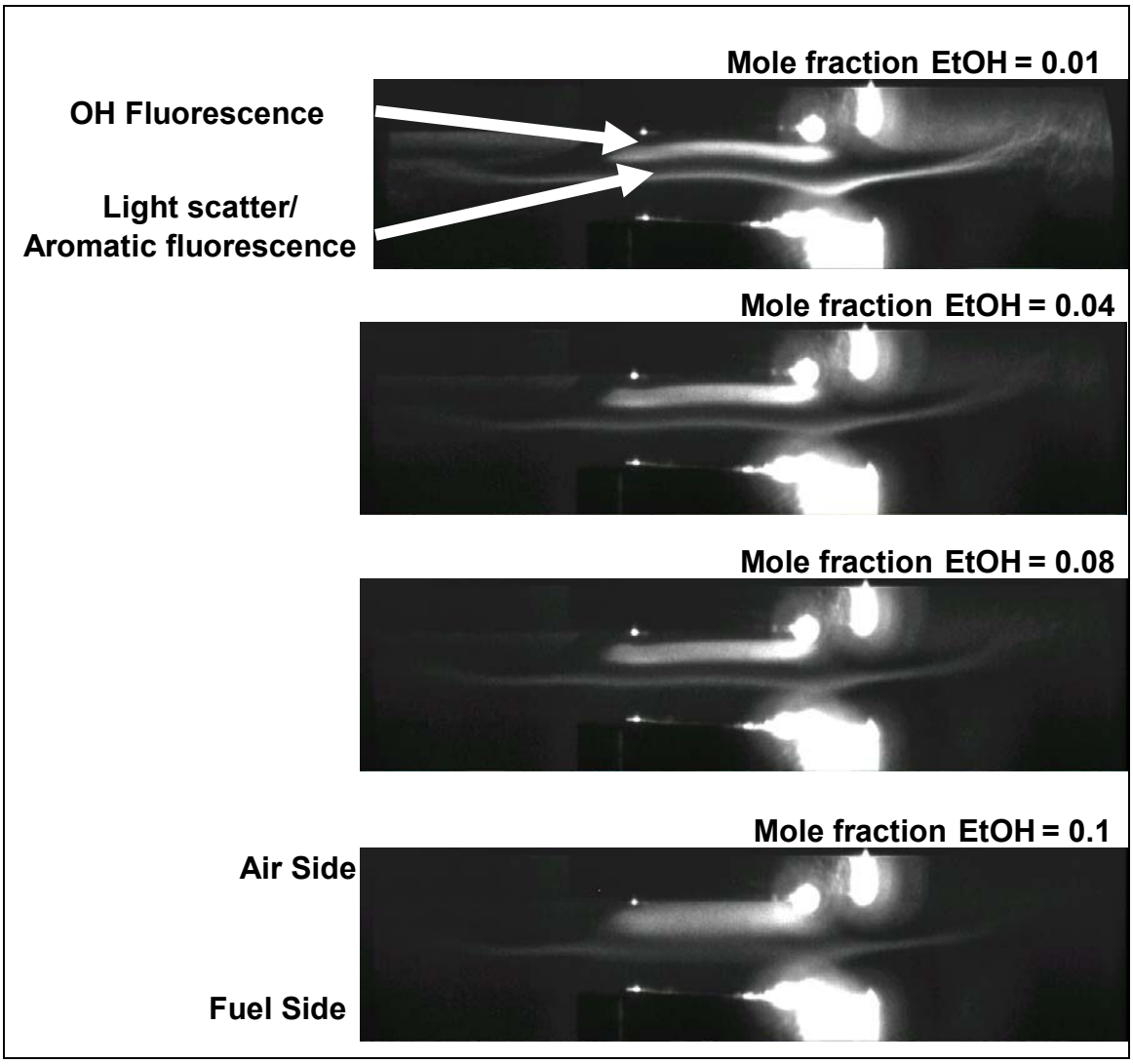

Figure 7. Images of OH PLIF and light scattering by soot particles as increasing amounts of ethanol vapor are added to the air side. Note increasing width of OH region (upper feature) and decreasing intensity of light scatter from particles (lower feature).

The OH and CO produced by the premixed ethanol/air flame are formed at a temperature near 1500 K and are then convected into the diffusion flame combustion region. The convection of the hot gases from the premixed flame into the diffusion flame region results in a preheating of the oxidizer side of the diffusion flame, raises peak flame temperature, and accounts for the broadened OH and temperature profiles in calculation and experiment (see figures 7–10).

Table 3 shows the calculated peak temperatures, calculated peak mole fractions, and integrated calculated mole fractions for several species identified as important for soot formation in tables 1 and 2, as ethanol addition to the oxidizer gas is varied up to 4% mole fraction. The table shows calculated values for air side ethanol addition up to 4%. Calculations beyond 4% used relaxed

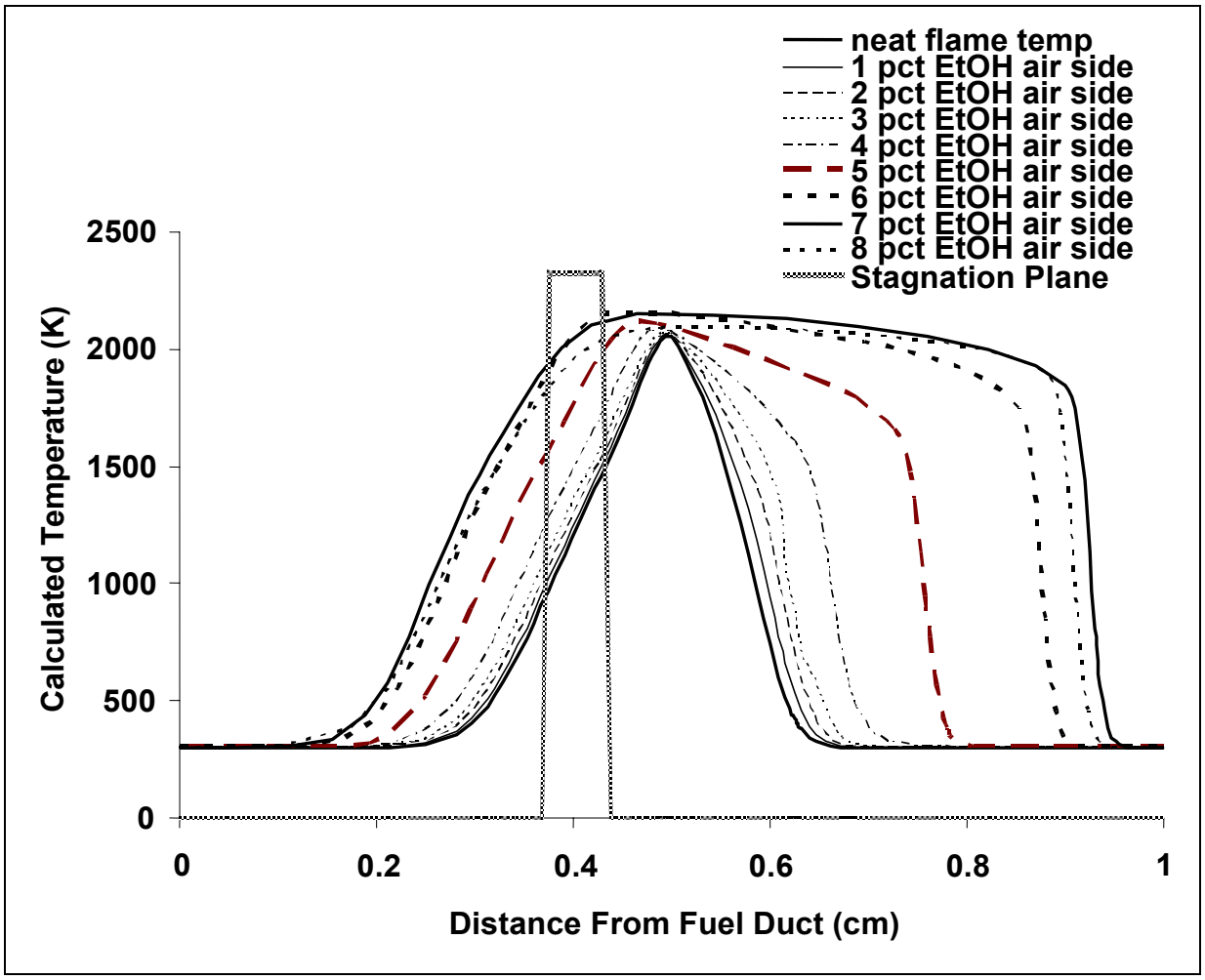

Figure 8. Calculated temperature profiles for air side addition of ethanol. Also shown is estimated position of stagnation plane.

convergence criteria, as mentioned earlier (only for air side addition). The integration of mole fraction was performed using Simpsons Rule (*29*) and extended over the full space between oxidizer and flame ducts. It appears that the observed and calculated decrease in soot and soot precursor concentration is due mainly to a combination of increased radical concentration and thermal effect caused by the preheating of the oxidizer gases occurring in the premixed part of the flame, raising calculated peak flame temperature (33 K, or 1.6%). Peak calculated mole fractions for all species in table 3 that are important for soot formation decrease, while the integrated calculated mole fractions for the flame propagating species H, O, and OH increase by 41%, 52%, and 142%, respectively. The effect of increased flame temperature on radical species concentrations is complicated by the accompanying broadening of the temperature profile. However, we believe the increase in OH integrated mole fraction as ethanol addition increases is indicative of a thermal effect on the net rate constant for OH formation. In addition to decreasing soot by increasing OH and increasing direct oxidation (see reaction 8), the thermal

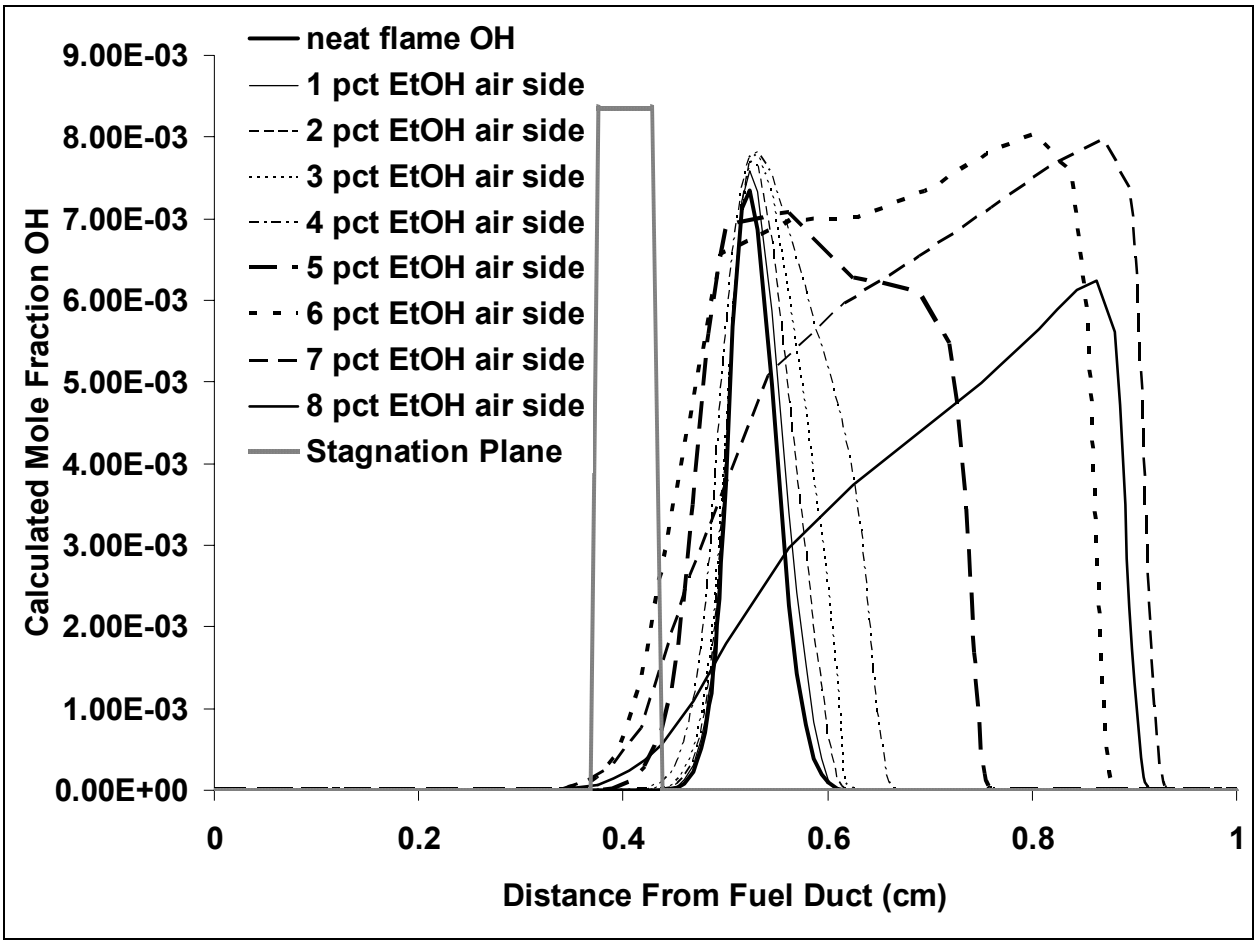

Figure 9. Calculated OH profiles for air side addition of ethanol. Also shown is estimated position of stagnation plane.

effect decreases A1 through A4 formation by increasing integrated OH and H mole fraction, decreasing the amount of CH_2 available for reaction to propargyl. Formation of propargyl (C_3H_3) is dependent upon the reaction

$$CH_2 + C_2H_2 \rightarrow C_3H_3 + H\ . \tag{9}$$

The rate of production of propargyl by this reaction decreases ~28% when the oxidizer contains 4% mole fraction ethanol.

4.3 Fuel Side Addition

In experiments and calculations, fuel side addition of ethanol increases soot and soot precursors, while peak OH concentrations remain approximately constant. A graph of experimental measurements of peak light scatter and OH fluorescence and predictions of species maximum mole fraction based upon calculations, for fuel side addition of ethanol, is shown in figure 11.

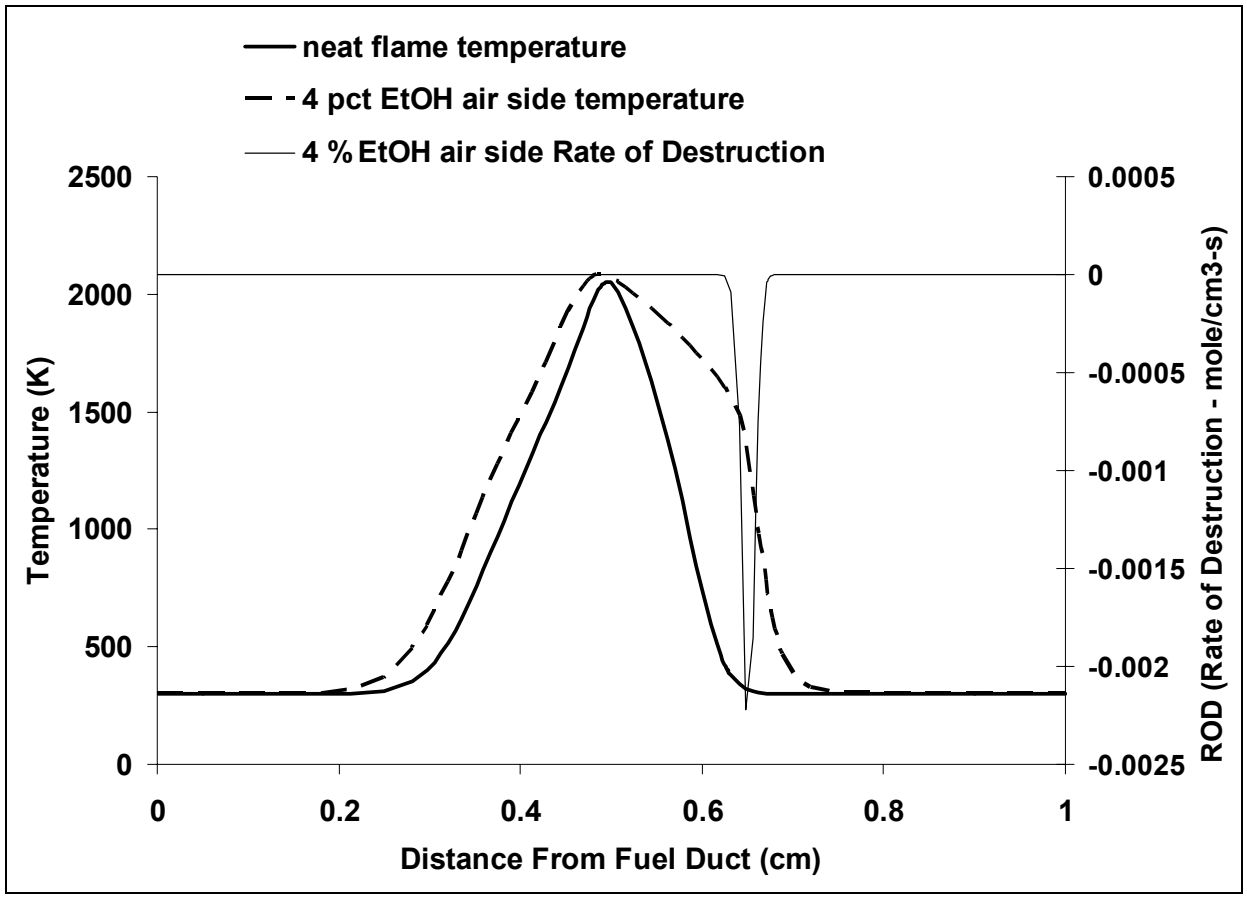

Figure 10. Calculated temperature profile for air side addition of ethanol, overlaid with overall rate of destruction of ethanol vapor (4% mole fraction fuel side). Note the coincidence of ethanol vapor combustion with edge of broadened temperature profile.

The calculated data have been normalized to the experimental data to allow comparisons of the trends shown by each. As in figure 6, the error in the measured scattered laser intensity and OH fluorescence is estimated to be ~5%, based upon pixel to pixel noise in the individual images. Overall, the trend of the change (increasing), with increasing fuel side ethanol addition, of calculated peak mole fractions for the species A1 through A4 is in good agreement with peak experimental values (measured along the centerline between burner ducts) of light scatter, while the change, with increasing fuel side ethanol addition, of the calculated peak mole fraction of OH is in reasonable agreement with peak measured values of OH fluorescence. Calculation and experimental measurement show peak OH concentration to remain nearly constant with increasing ethanol addition. For these flames, the calculation was able to reach convergence for all mole fractions of ethanol using an initial grid of 60 points. Individual experimental images do not show apparent differences so are not reproduced here.

Calculations predict that the addition of 8 mole % ethanol to the fuel stream increases the integrated mole fraction of aromatic species A1 (C_6H_6), A2 ($C_{10}H_8$), A3 ($C_{14}H_{10}$), and A4 ($C_{16}H_{10}$) by ~3%, 19%, 23%, and 22%, respectively (see figures 12–15). The peak increase

Table 2. Reaction path of ethanol to products for ethylene/air opposed flow diffusion flames that have ethanol vapor added to the air side. Important reactions contributing to each species concentration are shown to the right. Percentage value in parenthesis refers to the amount of species in bold consumed or produced by that reaction.

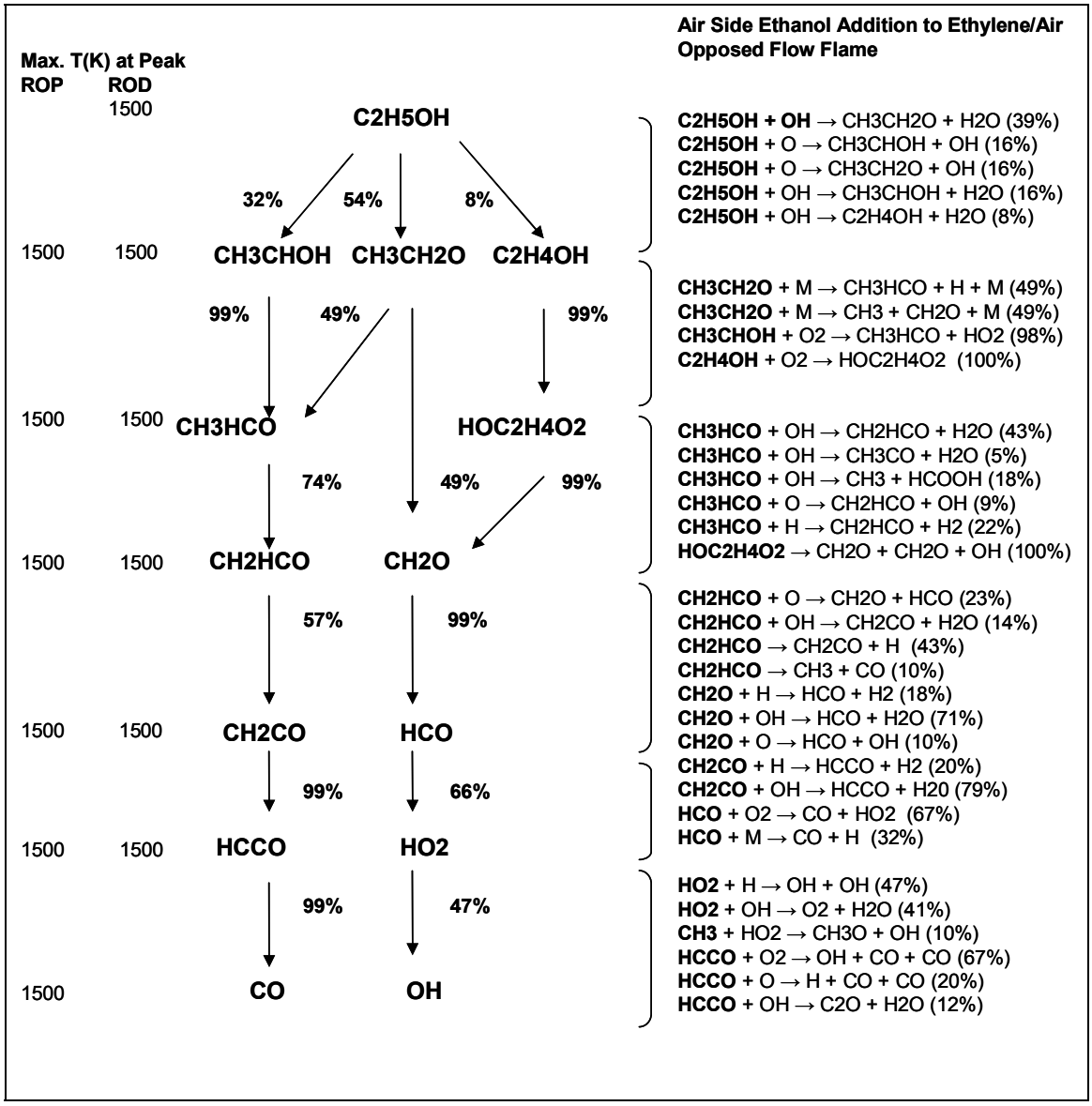

in light scatter observed experimentally was ~19%. Temperature and OH concentration are predicted by calculation to remain approximately constant (see figure 16). Acetylene is predicted to remain approximately constant while propargyl concentration is predicted to decrease ~9% when 8% ethanol is added to the fuel stream (figure 17). In what follows, the production of soot precursors is divided into a discussion of A1 formation followed by a discussion of A2–A4 formation.

Table 3. The calculated change in peak and integrated mole fraction for air side ethanol addition for H, O, OH, CH_2, C_2H_2, C_3H_3, n-C_4H_5, C_4H_6, A1, and A4. This table is presented to show that most species influencing A1 and A4 production are affected by air side addition of ethanol vapor.

Air Side Ethanol Addition						
Peak Mole Fraction; Integrated Mole Fraction (mole fraction-cm)						
	T (K)	**H (X 10^{-4})**	**O (X 10^{-4})**	**OH (X 10^{-4})**	**CH_2 (X 10^{-6})**	**—**
Mole frac. EtOH	—	—	—	—	—	—
0	2053	65; 3.97	52; 2.7	74; 3.93	57; 1.46	—
1	2058	62; 4.2	47; 2.8	76; 4.58	52; 1.44	—
2	2062	59; 4.4	44; 3.0	77; 5.41	47; 1.40	—
3	2068	54; 4.8	39; 3.3	77; 6.62	41; 1.38	—
4	2086	48; 5.6	32; 4.1	78; 9.5	35; 1.4	—
% change	+1.6	–26; +41	–63; +52	+5.4; +142	–38; –4	**—**
Peak Mole Fraction; Integrated Mole Fraction (mole fraction-cm)						
	C_2H_2 (X 10-2)	**C_3H_3 (X 10^{-6})**	**n-C_4H_5 (X 10^{-8})**	**C_4H_6 (X 10^{-4})**	**A1 (X 10^{-5})**	**A4 (X 10^{-9})**
Mole frac. EtOH	—	—	—	—	—	—
0	5.5; 0.651	104; 7.7	51; 2.39	27; 2.3	14; 1.44	25; 2.48
1	5.4; 0.655	97; 7.4	47; 2.27	27; 2.25	13; 1.35	19; 1.98
2	5.3; 0.658	90; 7.1	45; 2.14	27; 2.24	12; 1.25	15; 1.54
3	5.2; 0.66	82; 6.8	40; 2.01	26; 2.24	11; 1.15	11; 1.14
4	5.0; 0.67	75; 6.5	36; 1.87	26; 2.27	9.4; 1.03	7; 0.75
% change	–9; +3	–28; –16	–29; –22	–4; –1	–33; –28	–72; –70

4.3.1 A1 Formation

Because the calculated change in propargyl mole fraction with ethanol addition was in the opposite direction of the change in A1 mole fraction for fuel side ethanol addition, a calculation of rate of formation of A1 by reaction was performed. The reactions contributing to A1 formation, and the change in A1 rate of formation per reaction, relative to the neat flame, when 8% ethanol was added to the fuel stream, are as follows:

Reaction	**Calculated Change in Rate of A1 Formation - 8% EtOH addition to Fuel (relative to neat flame)**
$C_3H_3 + C_3H_3 \rightarrow A1$	–8%
n-C4H5 + C2H2 → A1 + H	+23%
l-C6H6 + H → A1 + H	+27%
n-C6H7 → A1 + H	+34%

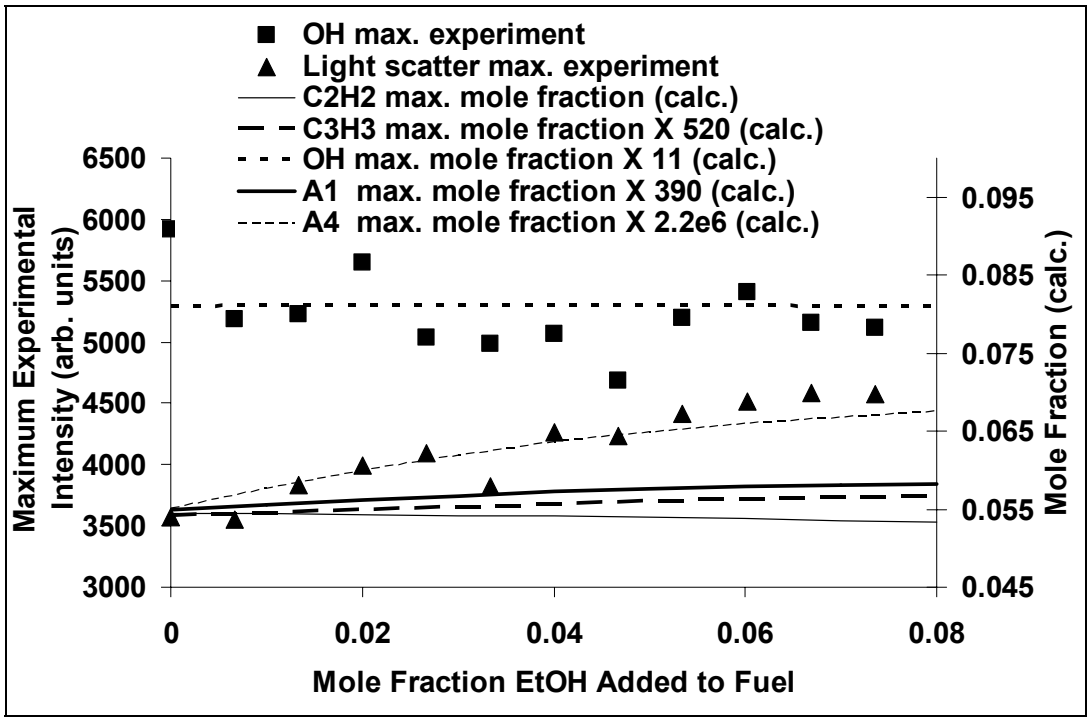

Figure 11. Graph of experimental measurements and predictions based upon calculations for OH, soot, and soot precursors, for fuel side addition of ethanol.

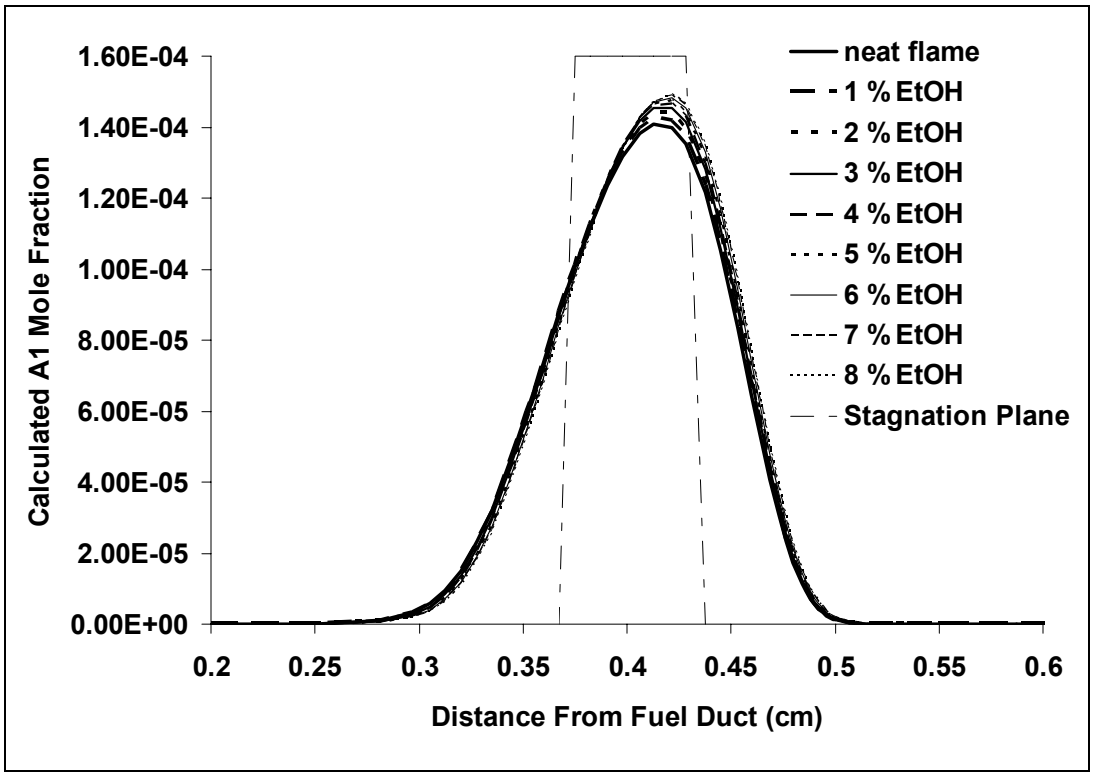

Figure 12. Calculated A1 mole fraction profile for increasing amounts of ethanol vapor added to the fuel stream.

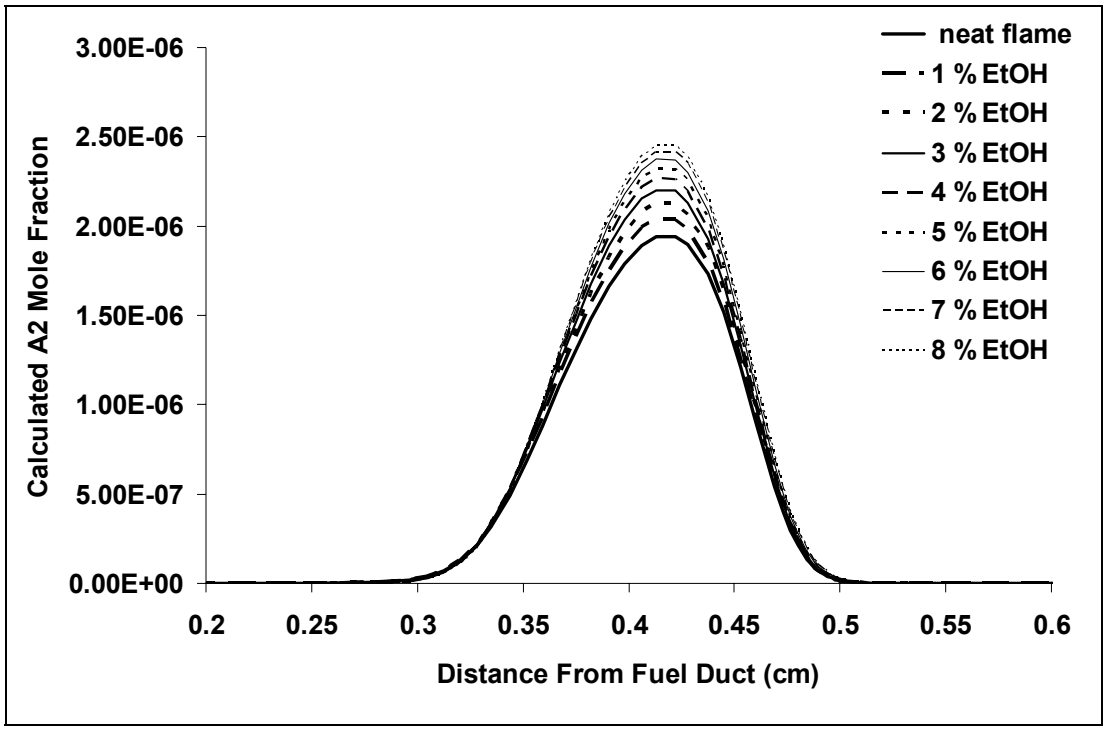

Figure 13. Calculated A2 mole fraction profile for increasing amounts of ethanol vapor added to the fuel stream.

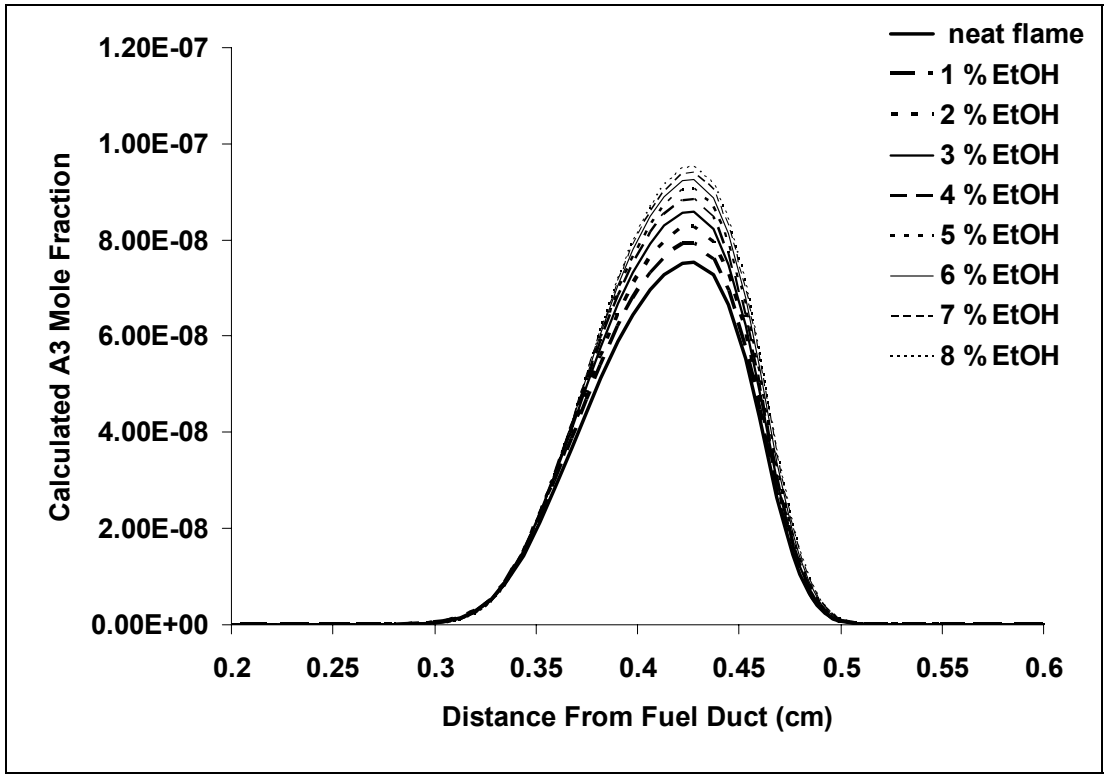

Figure 14. Calculated A3 mole fraction profile for increasing amounts of ethanol vapor added to the fuel stream.

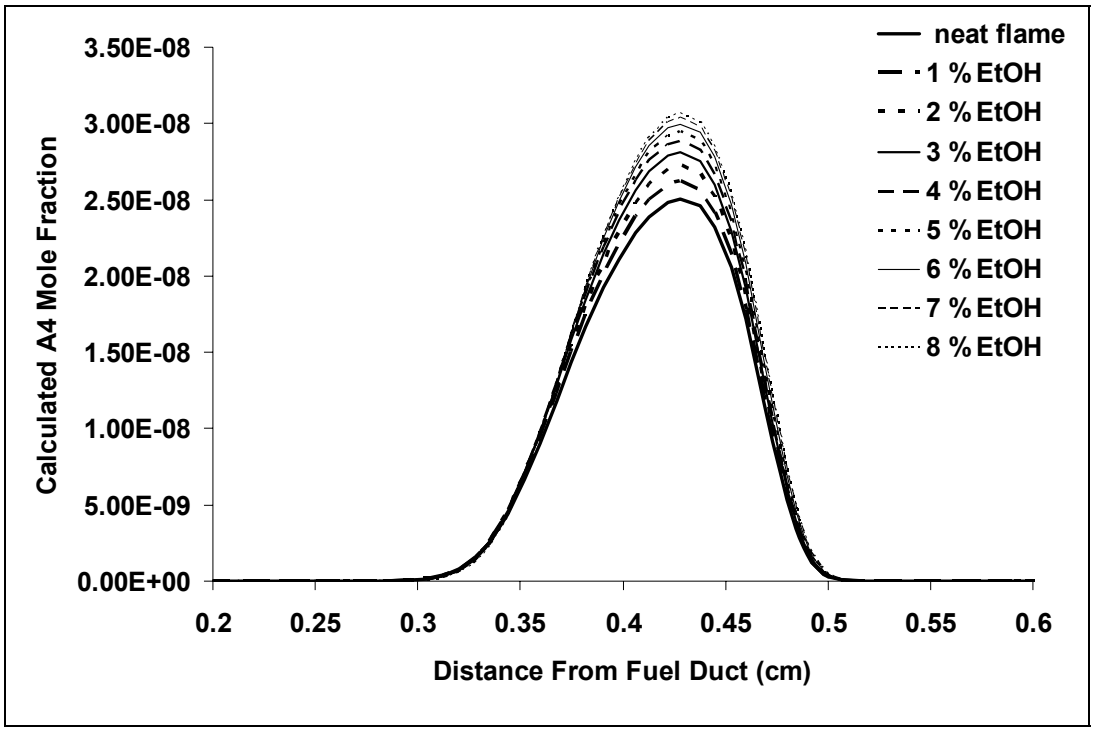

Figure 15. Calculated A4 mole fraction profile for increasing amounts of ethanol vapor added to the fuel stream.

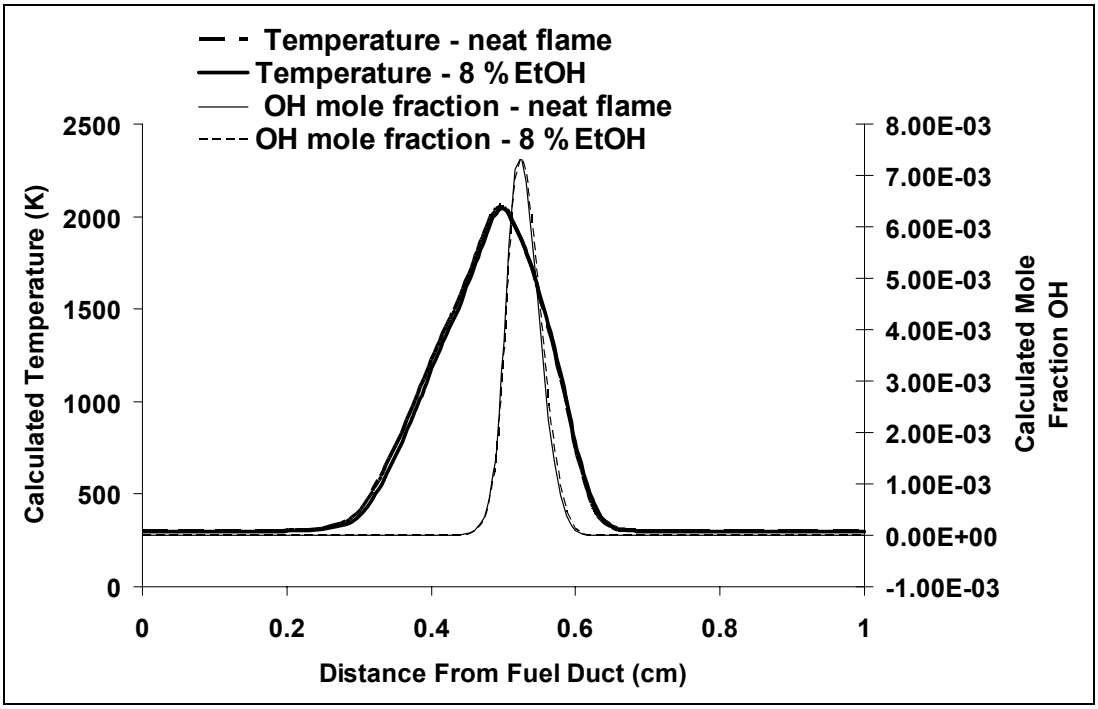

Figure 16. Calculated temperature and OH profiles for neat flames and for flames with 8% ethanol vapor added to the fuel stream. Intermediate values of ethanol addition yield temperatures and OH profiles between those for the extreme values. Note that the calculation predicts negligible change in OH and temperature for fuel side addition of ethanol.

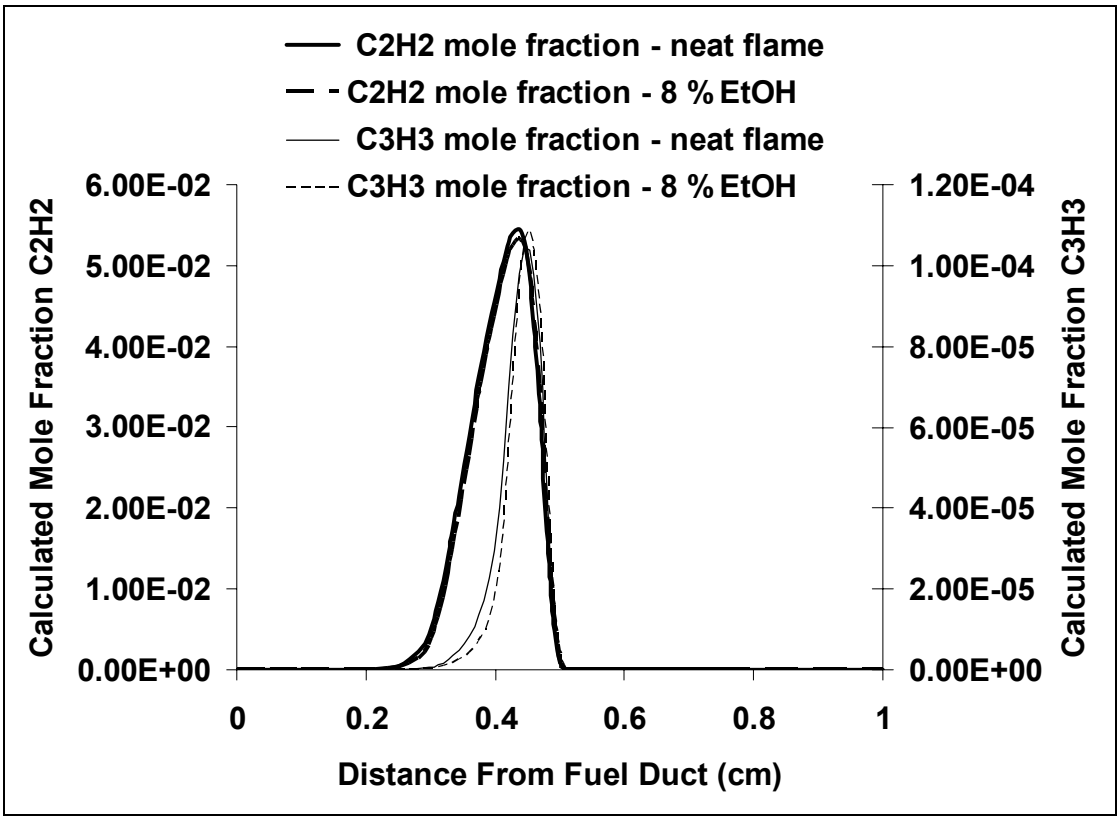

Figure 17. Calculated acetylene (C_2H_2) and propargyl (C_3H_3) profiles for increasing amounts of ethanol vapor added to the fuel stream. Note that the calculation predicts negligible change in acetylene and very small decrease in propargyl for fuel side addition of ethanol.

The calculation predicts that all of the increase in A1 produced by fuel side ethanol addition is caused by reactions other than propargyl recombination. The reactions of phenyl (A1·) influencing A1 formation,

$$A1\cdot + H\ (+M) \rightarrow A1\ (+M) \tag{10}$$

and

$$A1 + OH \rightarrow A1 + H_2O\ , \tag{11}$$

are included in the mechanism but are not considered important here for A1 formation because the change in rate of each was less than 1% with fuel side ethanol addition.

To understand why propargyl is decreased, and why reactions 5–7 are enhanced, it is necessary to track the path of oxygen and carbon added, via ethanol, to the fuel gas. A listing of the reactions responsible for the increase in soot formation for fuel side ethanol addition, predicted by the calculations, may be found in table 4. The initial decomposition reactions for ethanol when added on the fuel side of the flame differ from those for air side ethanol addition (see table 2).

Table 4. Reaction path of ethanol to products for ethylene/air opposed flow diffusion flames that have ethanol vapor added to the fuel side. Important reactions contributing to each species concentration are shown to the right. Percentage value in parenthesis refers to the amount of species in bold consumed or produced by that reaction.

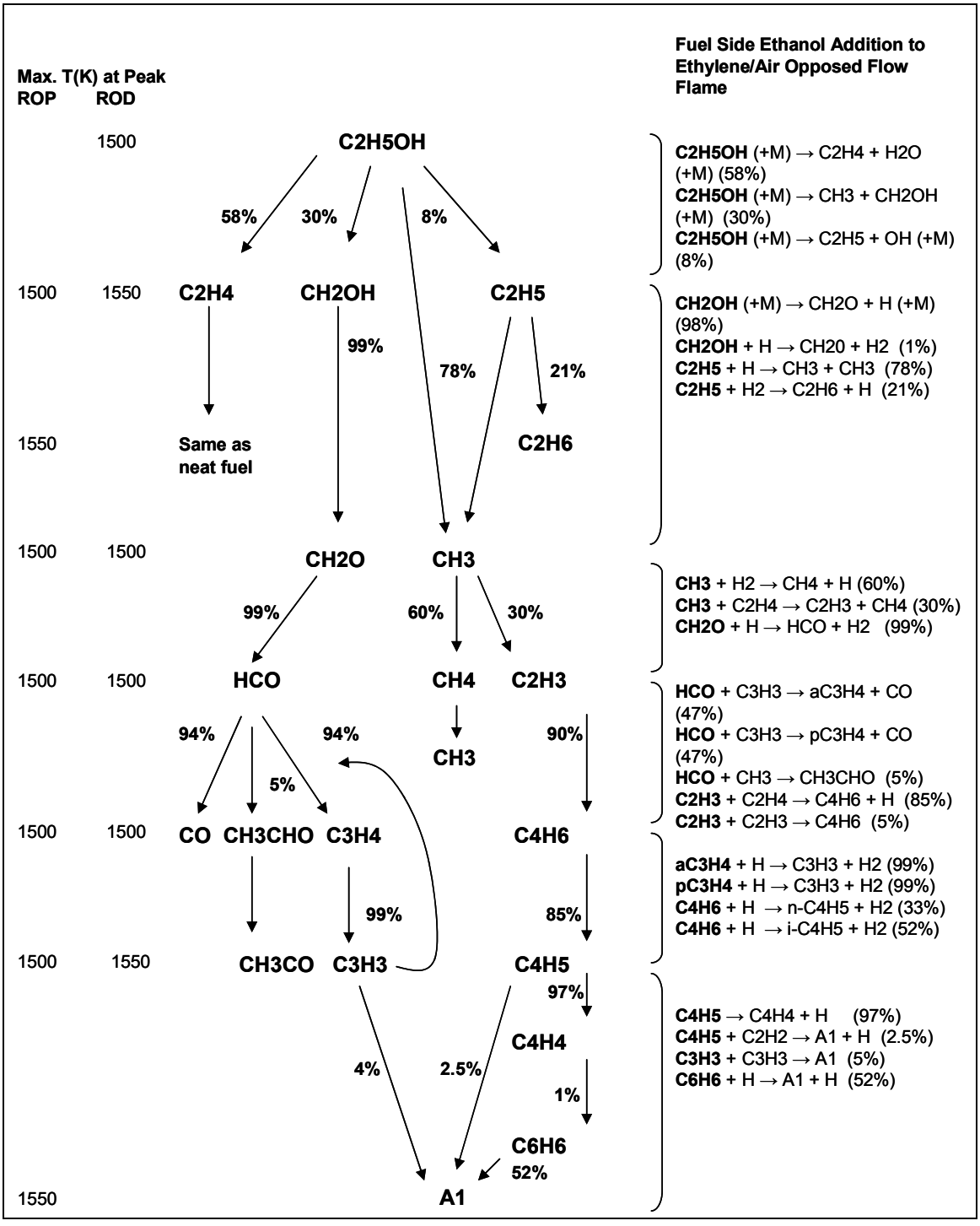

For fuel side addition, in the absence of oxygen, ethanol decomposition occurs via a pyrolysis mechanism at approximately 1500 K:

$$C_2H_5OH\ (+M) \rightarrow C_2H_4 + H_2O\ (+M) \qquad 58\% \qquad (12)$$

$$C2H5OH\ (+M) \rightarrow CH3 + CH2OH\ (+M) \qquad 30\% \qquad (13)$$

$$C2H5OH\ (+M) \rightarrow C2H5 + OH\ (+M) \qquad 8\% \qquad (14)$$

The ethylene, water, ethyl radical, and OH radical formed from the initial decomposition have little additional effect on the chemistry as they are very slight perturbations on the concentrations of these species relative to the neat flame (see figures 13 and 14) or are similar to fuel or initial fuel decomposition products. The bulk of the reactive oxygen (as CH_2OH) is stepwise converted to HCO, which then reacts with propargyl to yield CO and C_3H_4, which is then near-quantitatively reconverted to propargyl. The increase in other soot precursors (*6*) predicted by the calculation may be ascribed to introduction of methyl radical (reaction 13) into a relatively low temperature hydrocarbon/acetylene bath (*14*).

The methyl radicals formed in cooler regions of the flame (1400 K–1700 K) via ethylene pyrolysis react with propargyl (C_3H_3) to form C_4H_6:

$$C_3H_3 + CH_3\ (+M) \rightarrow C_4H_6\ (+M)\ . \qquad (15)$$

This reaction shows a calculated increase in rate of production of C_4H_6 of 17% for the flame with 8% mole fraction ethanol compared to the neat ethylene/air flame. Mole fraction profiles (see figure 17) of propargyl show a slight decrease in concentration over this temperature range (1400–1700 K). Approximately 85% of the C_4H_6 reacts with H to form C_4H_5, which then reacts in the acetylene bath to form A1 and aromatic precursors.

$$C_4H_6 + H \rightarrow C_4H_5 + H_2\ . \qquad (16)$$

$$C_4H_5 + C_2H_2 \rightarrow A1 + H\ . \qquad (17)$$

$$C_4H_5 + C_2H_2 \rightarrow n\text{-}C_6H_7\ . \qquad (18)$$

Overall, the calculation predicts that the addition of ethanol to the fuel stream has a negative effect on integrated C_3H_3 concentration while enhancing alternate pathways, via C_4H_6 production, to formation of initial aromatic ring species (see figure 18). This result was not anticipated prior to the experimental studies. However, it should be noted that other researchers (*9*) have measured soot increases during combustion of ethanol/hydrocarbon mixtures, relative to neat ethylene combustion. Increases in soot precursor production have also been reported for methane addition to heptane /air flames (*30*).

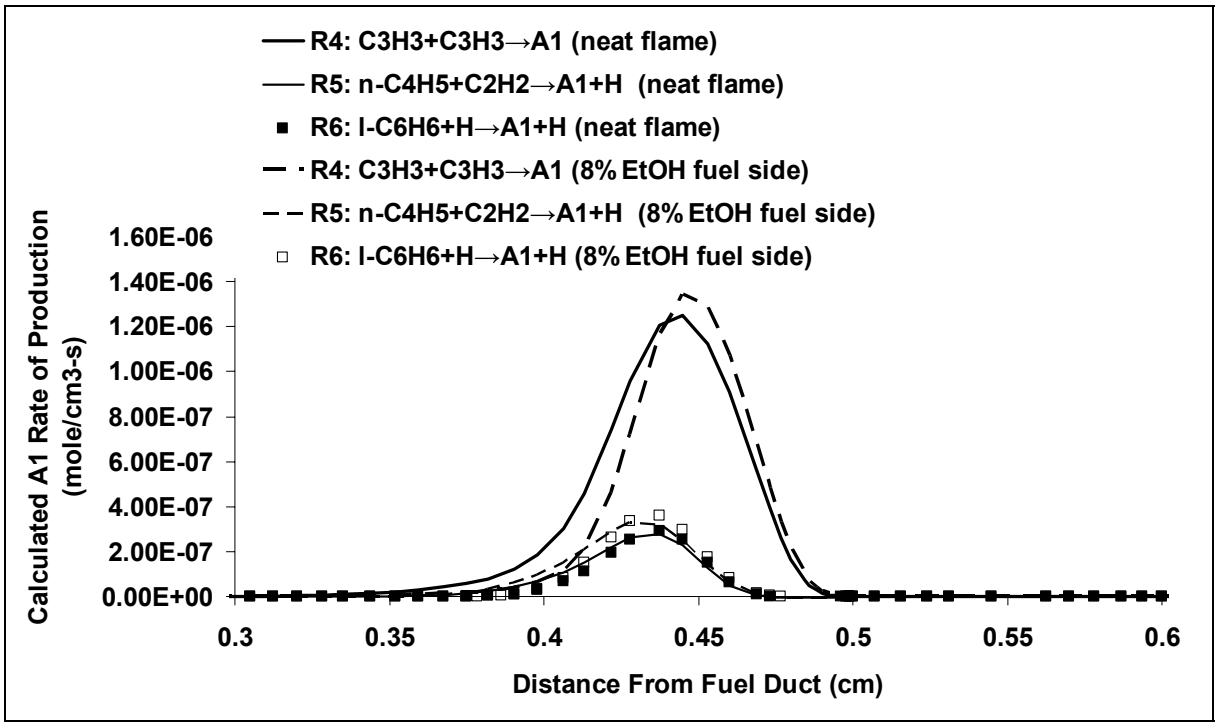

Figure 18. Rates of production of A1 by the three most important reactions contributing to A1 production. Note the enhancement of rates of reactions that do not involve propargyl.

4.3.2 A2–A4 Formation

For fuel side ethanol addition, the calculation predicts an increase in integrated mole fraction of benzene of 3% when 8% ethanol is added, relative to the neat flame. For the same comparison, the predicted increase in A2 (naphthalene), A3 (phenanthrene), and A4 (pyrene) is 19%, 23%, and 22%, respectively (see figures 12–15). However, the absolute change in mole fraction of A1 with 8% fuel side ethanol addition is greater than 10× the absolute change in A2 addition. The change in mole fraction in going from the neat flame to the flame with 8% ethanol added to the fuel side for A1, A2, A3, and A4 is 5×10^{-7}, 4.2×10^{-8}, 1.6×10^{-9}, and $4.8 \times 10\text{-}^{10}$, respectively. In contrast to the reaction path to A1 formation discussed, the formation of A2–A4 follows the H-abstraction – C2H2-addition mechanism (*31*). For A1 conversion to A2, an example of one of the pathways is summarized in figure 19.

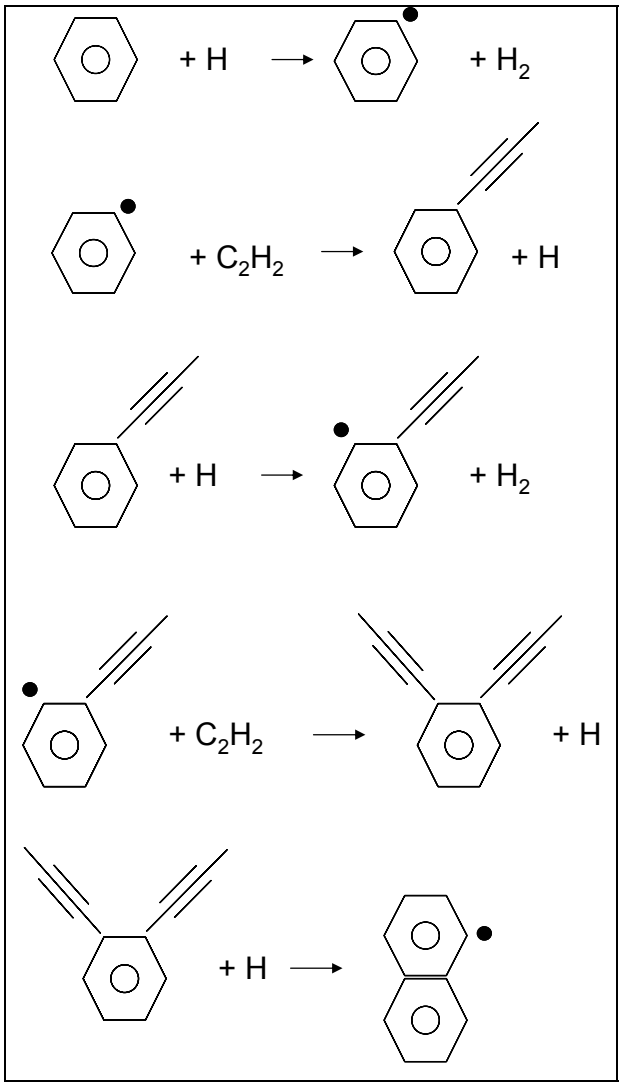

Figure 19. Example of pathway for A1 conversion to A2.

5. Conclusion

This study provides an example of how soot formation in opposed flow ethylene/air diffusion flames is dependent upon temperature, flame radical, and bath gas compositions. Differing chemical behavior in opposed flow flames depending on fuel or air side addition of ethanol vapor has been observed experimentally and modeled, and shown to occur via different pathways within the context of a detailed chemical mechanism. In particular, ethanol introduced into the air side of the flame creates a premixed combustion (secondary flame zone) region prior to the main diffusion flame region. Hot gas products from this premixed flame region, including OH,

are convected into the diffusion flame zone, increasing peak temperature, and broadening the OH concentration profile. The broadened OH concentration profile moves the oxidizing region of the flame closer to the stagnation plane and to the high soot concentration region of the flame. The increased temperature and integrated OH mole fraction cause an increase in soot and soot-precursor oxidation, leading to lower overall soot concentrations in ethylene/air diffusion flames with ethanol added to the air stream. It should be noted that the effect of radiation from soot in the experiment was not accounted for in the "particle-free" computational model.

When ethanol is introduced into the fuel stream of the ethanol/air opposed flow diffusion flame, initial decomposition of ethanol occurs via pyrolysis reactions because of the lack of oxygen in the fuel stream. Methyl radical produced during the initial steps of decomposition of ethanol reacts with propargyl to produce C_4H_6, which leads to increased production of A1.

In summary, we believe addition of ethanol to the air side of the ethylene/air diffusion flame decreases soot concentration mainly through a thermal mechanism. This is supported by observation of the flame and the calculated increase in temperature (33 K) and increase in OH concentration (142%) relative to the neat flame. Addition of ethanol to the fuel side of the ethylene/air diffusion flame increases soot mainly through a chemical mechanism involving introduction of methyl radical into an ethylene/acetylene bath. This is supported by observation of the flame and the calculated constant temperature and OH concentrations over the studied range of ethanol addition.

6. References

1. Howard, R. P.; Hiers, R. S.; Whitefield, P. D. Jr.; Hagen, D. E.; Wormhoudt, J. C.; Miake-Lye, R. C.; Strange, R. *Experimental Characterization of Gas Turbine Emissions at Simulated Altitude Conditions*; AEDC-TR-96-3; USAF Arnold Engineering Development Center: Arnold AFB, TN, September 1996.

2. Dockery, D. W.; Pope, C. A.; Xu, X. An Association Between Air Pollution and Mortality in Six Cities. *New England Journal of Medicine* **1993**, *329*, 1753–1759.

3. Dennisenko, M. F.; Pao, A.; Tang, M. S.; Pfeifer, G. P. Preferential Formation of benzo[a]pyrene Adducts at Lung Cancer Mutational Hotspots in P53. *Science* **1996**, *273*, pp 430–432.

4. Niedzwiecki, R. *Aircraft Technology and its Relation to Emissions*; chapter 7 of report of The Intergovernmental Panel on Climate Change, IPCC, submitted for publication.

5. *Reduced PM2.5 Emissions for Military Gas Turbine Engines Using Fuel Additives*; administered by the Strategic Environmental Research and Development Program (DOD, EPA, DOE).

6. Richter, H.; Howard, J. B. Formation of Polycyclic Aromatic Hydrocarbons and Their Growth to Soot—A Review of Chemical Reaction Pathways, *Progress in Energy and Combustion Science* **2000**, *26*, 565–608.

7. Colket, M. B.; Hall, R. J. *Soot Formation in Combustion*; Bockhorn, H., Ed.; Springer Verlag: Berlin, Germany, 1994; p 417.

8. Glassman, I. *Combustion*; 3rd ed.; Academic Press: New York, NY, 1987; pp 360–375.

9. Alexiou, A.; Williams, A. Soot Formation in Shock Tube Pyrolysis of Toluene, Toluene-Methanol, Toluene-Ethanol, and Toluene-Oxygen Mixtures. *Combustion and Flame* **1996**, *104*, 51–65.

10. Appel, J.; Bockhorn, H.; Frenklach, M. Y. Kinetic Modeling of Soot Formation With Detailed Chemistry and Physics. *Laminar Premixed Flames of C_2 Hydrocarbons, Combustion and Flame* **2000**, *121*, 122–136.

11. Hall, R. J.; Smooke, M. D.; Colket, M. B. Predictions of Soot Dynamics in Opposed Jet Diffusion Flames. In *Physical and Chemical Aspects of Combustion—A Tribute to Irvin Glassman*; Dryer, F. L., Sawyer, R. F., Eds.; Gordon and Breach Science Publishers: The Netherlands, 1997; pp 189–230.

12. Welle, E. J.; Roberts, W. L.; Careter, C. D.; Donbar, J. M. The Response of a Propane-Air Counter-Flow Diffusion Flame Subjected to a Transient Flow Field. *Combustion and Flame* **2003**, *135*, 285–297.

13. Shaddix, C. R.; Smyth, K. C. Laser-Induced Incandescence Measurements of Soot Production in Steady and Flickering Methane, Propane, and Ethylene Diffusion Flames. *Combustion and Flame* **1996**, *107*, 418–452.

14. Hwang, J. Y.; Chung, S. H. Growth of Soot Particles in Counterflow Diffusion Flames of Ethylene. *Combustion and Flame* **2001**, *125*, 752–762.

15. Rumminger, M. D.; Linteris, G. T. The Role of Particles in the Inhibition of Counterflow Diffusion Flames by Iron Pentacarbonyl. *Combustion and Flame* **2002**, *128*, 145–164.

16. Du, D. X.; Wang, H.; Law, C. K. Soot Formation in Counterflow Ethylene Diffusion Flames From 1 to 25 Atmospheres. *Combustion and Flame* **1988**, *113*, 264–270.

17. Lentati, A. M.; Chelliah, H. K. Dynamics of Water Droplets in a Counterflow Field and Their Effect on Flame Extinction. *Combustion and Flame* **1998**, *115*, 158–179.

18. Harris, S. J.; Kennedy, I. M. The Coagulation of Soot Particles With Van der Waals Forces. *Combustion Science and Technology* **1988**, *59*, 443–454.

19. Smyth, K. C.; Shaddix, C. R.; Everest, D. A. Aspects of Soot Dynamics as Revealed by Measurements of Broadband Fluorescence and Flame Luminosity in Flickering Diffusion Flames. *Combustion and Flame* **1997**, *111*, 185–207.

20. Howard, J. B.; Kausch, W. J. Soot Control by Fuel Additives. *Progress Energy Combustion Science* **1980**, *6*, 263–276.

21. Kang, K. T.; Hwang, J. Y.; Chung, S. H. Soot Zone Structure and Sooting Limit in Diffusion Flames, Comparison of Counterflow and Co-Flow Flames. *Combustion and Flame* **1997**, *109*, 266–281.

22. Reist, P. C. *Aerosol Science and Technology*, 2nd ed.; McGraw Hill: New York, NY, 1993; pp 263–275.

23. Song, K. H.; Nag, P.; Litzinger, T. A.; Haworth, D. C. Effects of Oxygenated Additives on Aromatic Species in Fuel-Rich, Premixed Ethane Combustion: A Modeling Study. *Combustion and Flame* **2003**, *135*, 341–349.

24. Calcote, H. F. Mechanisms of Soot Nucleation in Flames. *Combustion Flame* **1981**, *42*, 215–242.

25. Haynes, B. S.; Wagner, H. G. Soot Formation. *Progress in Energy and Combustion Science* **1981**, *7*, 229–273.

26. Sung, C. J.; Kistler, J. S.; Nishioka, M.; Law, C. K. Further Studies on Effects of Thermophoresis on Seeding Particles in LDV Measurements of Strained Flames. *Combustion and Flame* **1996**, *105*, 189–201.

27. Shaddix, C. R.; Harrington, J. E.; Smyth, K. C. Quantitative Measurements of Enhanced Soot Production in a Flickering Methane/Air Diffusion Flame. *Combustion and Flame*, **1994**, *99*, 723–732 .

28. Lockett, R. D.; Boulanger, B.; Harding, S. C.; Greenhalgh, D. A. The Structure and Stability of the Laminar Counter-Flow Partially Premixed Methane/Air Triple Flame. *Combustion and Flame*, **1999**, *119*, 109–120.

29. Abramowitz, M.; Stegun, I. A., Eds. *Handbook of Mathematical Functions With Formulas, Graphs, and Mathematical Tables*; Dover: New York, NY, 1972, p 886.

30. Roesler, J. F.; Martinot, S.; McEnally, C. S.; Pfefferle, L. D.; Delfau, J. L.; Vovelle, C. Investigating the Role of Methane on the Growth of Aromatic Hydrocarbons and Soot in Fundamental Combustion Processes. *Combustion and Flame* **2003**, *134*, 249–260.

31. Wang, H.; Frenklach, M. A Detailed Kinetic and Modeling Study of Aromatics Formation in Laminar Premixed Acetylene and Ethylene Flames. *Combustion and Flame* **1997**, *110*, 173–221.

NO. OF COPIES ORGANIZATION

1 (PDF ONLY) DEFENSE TECHNICAL INFORMATION CTR
DTIC OCA
8725 JOHN J KINGMAN RD
STE 0944
FORT BELVOIR VA 22060-6218

1 US ARMY RSRCH DEV & ENGRG CMD
SYSTEMS OF SYSTEMS INTEGRATION
AMSRD SS T
6000 6TH ST STE 100
FORT BELVOIR VA 22060-5608

1 INST FOR ADVNCD TCHNLGY
THE UNIV OF TEXAS
AT AUSTIN
3925 W BRAKER LN STE 400
AUSTIN TX 78759-5316

1 US MILITARY ACADEMY
MATH SCI CTR EXCELLENCE
MADN MATH
THAYER HALL
WEST POINT NY 10996-1786

1 DIRECTOR
US ARMY RESEARCH LAB
IMNE ALC IMS
2800 POWDER MILL RD
ADELPHI MD 20783-1197

3 DIRECTOR
US ARMY RESEARCH LAB
AMSRD ARL CI OK TL
2800 POWDER MILL RD
ADELPHI MD 20783-1197

3 DIRECTOR
US ARMY RESEARCH LAB
AMSRD ARL CS IS T
2800 POWDER MILL RD
ADELPHI MD 20783-1197

NO. OF COPIES ORGANIZATION

ABERDEEN PROVING GROUND

1 DIR USARL
AMSRD ARL CI OK TP (BLDG 4600)

NO. OF COPIES	ORGANIZATION
1	AIR FORCE RESEARCH LAB EDWARDS (AFRL) AFRL EDWARDS/USC ERC/AFRL K CRISTE 10 E SATURN BLVD EDWARDS AFB CA 93524
1	AIR FORCE RESEARCH LAB AFRL/PRSP BLDG 8451 G DRAKE 10 EAST SATURN BLVD EDWARDS AFB CA 93524
1	AIR FORCE RESEARCH LAB EGLIN (AFRL) AFRL/MNME W COOPER 2306 PERIMETER RD EGLIN AFB FL 32542
1	AIR FORCE RESEARCH LAB AFRL/MNME M FAJARDO 2306 PERIMETER RD EGLIN AFB FL 32542
1	AIR FORCE RESEARCH LAB AFRL/MNAV S FEDERLE 101 W EGLIN BLVD STE 342 EGLIN AFB FL 32542
1	AIR FORCE RESEARCH LAB AFRL/MN S KORN 101 W EGLIN BLVD STE 105 EGLIN AFB FL 32542-6810
1	AIR FORCE RESEARCH LAB AFRL/MNME M KRAMER 2306 PERIMETER RD EGLIN AFB FL 32542-6810
1	AIR FORCE RESEARCH LAB AFRL/MNAC J KUJALA 101 WEST EGLIN BLVD STE 334 EGLIN AFB FL 32542-6810
1	AIR FORCE RESEARCH LAB AFRL/MNME W R MAINES 2306 PERIMETER RD EGLIN AFB FL 32542
1	AIR FORCE RESEARCH LAB AFRL/MNME T MCKELVEY 2306 PERIMETER RD EGLIN AFB FL 32542-5910
1	AIR FORCE RESEARCH LAB AFRL/MNME D W RICHARDS 2306 PERIMETER RD EGLIN AFB FL 32542
1	AIR FORCE RESEARCH LAB AFRL/MNME C RUMCHIK 2306 PERIMETER RD EGLIN AFB FL 32542
1	AIR FORCE RESEARCH LAB AFRL/MNME L STEWART 2306 PERIMETER RD EGLIN AFB FL 32542
1	AIR FORCE RESEARCH LAB AFRL/MNME K WALKER 2306 PERIMETER RD EGLIN AFB FL 32542
1	AIR FORCE AFOSR M BERMAN AFOSR 4015 WILSON BLVD RM 713 ARLINGTON VA 22203-1954
1	US ARMY ARDEC/WECAC D DOWNS AMSTA AR WEE/B3022 PICATINNY ARSENAL NJ 07806-5000
1	US ARMY TACOM ARDEC P HAN BLDG 3022 PICATINNY ARSENAL NJ 07806-5000

NO. OF COPIES	ORGANIZATION
1	US ARMY TACOM ARDEC L HARRIS AMSTA AR WEE A PICATINNY ARSENAL NJ 07806
1	US ARMY TACOM ARDEC D KAPOOR AMSTA AR WEA BLDG 355 PICATINNY ARSENAL NJ 07806
1	US ARMY TACOM ARDEC J LANNON AMSTA AR WE BLDG 1 PICATINNY ARSENAL NJ 07806-5000
1	US ARMY TACOM ARDEC S NICOLICH AMSTA AR WEE/B3022 PICATINNY ARSENAL NJ 07806-5000
1	US ARMY TACOM ARDEC R PAWLICKI DOTC BUILDING 3022 RM 222 PICATINNY ARSENAL NJ 07806-5000
1	US ARMY TACOM ARDEC V STEPANOV BLDG 3028 PICATINNY ARSENAL NJ 07806
1	US ARMY TACOM ARDEC R SURAPANENI BLDG 3022 PICATINNY ARSENAL NJ 07806-5000
1	COMMANDER US ARMY TACOM ARDEC T VLADIMIROFF AMSTA AR WEE A PICATINNY ARSENAL NJ 07806
1	COMMANDER US ARMY AMRDEC US AVIATION & MISSILE COMMAND AMSAM RD PS PT R HATCHER REDSTONE ARSENAL AL 35989
1	US ARMY RESEARCH OFFICE D MANN PO BOX 12211 RESEARCH TRIANGLE PARK NC 27709-2211
1	COMMANDER US ARMY AMRDEC US AVIATION AND MISSILE COMMAND AMSAM RD PS WF S HILL REDSTONE ARSENAL AL 35898-5247
1	COMMANDER US ARMY AMRDEC US AVIATION AND MISSILE COMMAND AMSAM RD PS WF A STULTS REDSTONE ARSENAL AL 5989-5247
1	COMMANDER US ARMY AMRDEC US AVIATION AND MISSILE COMMAND AMSAM RD PS PT BLDG 7120 D THOMPSON REDSTONE ARSENAL AL 35989
1	NGIC IANG GS MT/MS 306 C BEITER 2055 BOULDERS RD CHARLOTTESVILLE VA 22911-8318
1	NGIC IANG GS MT/MS 306 R YOBS 2055 BOULDERS RD CHARLOTTESVILLE VA 22911-8318
1	COMMANDER US ARMY SOLDIER SYSTEMS CTR AMSSB RIP B (N) M MAFFEO NATICK MA 01760-5019
1	COMMANDER US ARMY SOLDIER SYSTEMS CTR AMSSB RIP B (N) J WARD NATICK MA 01760-5019

NO. OF COPIES	ORGANIZATION
1	US ARMY SPECIAL OPERATIONS COMMAND CAG COMBAT APPLICATIONS GROUP L BOIVIN PO BOX 70660 FT BRAGG NC 28307
1	US ARMY SPECIAL OPERATIONS COMMAND CAG COMBAT APPLICATIONS GROUP G GEORGEVITCH PO BOX 71859 FT BRAGG NC 28307-5000
1	US ARMY SPECIAL OPERATIONS COMMAND CAG COMBAT APPLICATIONS GROUP D JETER PO BOX 70660 FT BRAGG NC 28307
1	US MARINE CORPS CTR FOR EMERGING THREATS AND OPPORTUNITIES C CURCIO 3087 ROAN AVE BLDG 3087C QUANTICO VA 22134
1	US MARINE CORPS MARINE CORPS SYS COMMAND CESS PM NBC DEFENSE MEDICAL MCSC MED T EAGLES 20333 BARNETT AVE STE 315 QUANTICO VA 22134-5010
1	NAWC NAVAIR WEAPONS DIV J BALDWIN 1 ADMINISTRATION CIRCLE CODE 477200D CHINA LAKE CA 93555-6100
1	NAWC NAVAIR WEAPONS DIV T BOGGS CODE 4T4300D CHINA LAKE CA 93555-6100
1	NAWC NAVAIR WEAPONS DIV CODE 4T4310D M CHAN CHINA LAKE CA 93555-6100
1	NAWC NAVAIR WEAPONS DIV CODE 4T4200D R CHAPMAN CHINA LAKE CA 3555-6100
1	NAWC NAVAIR WEAPONS DIV 1 ADMINISTRATION CIRCLE CODE 478400D P DIXON CHINA LAKE CA 93555-6100
1	NAWC NAVAIR WEAPONS DIV T FOLEY 1 ADMINISTRATION CIRCLE CHINA LAKE CA 93555-6100
1	NAWC NAVAIR WEAPONS DIV K HIGA 1 ADMINISTRATION CIRCLE CHINA LAKE CA 93555-6100
1	NAWC NAVAIR WEAPONS DIV CODE 477200D B LORMAND 1 ADMINISTRATION CIRCLE CHINA LAKE CA 93555-6100
1	NAWC NAVAIR WEAPONS DIV CODE 477200D M MASON 1 ADMINISTRATION CIRCLE CHINA LAKE CA 93555-6100
1	NAWC NAVAIR WEAPONS DIV CODE 4T4320D T PARR CHINA LAKE CA 93555-6100

NO. OF COPIES	ORGANIZATION
1	NAVAL ORDNANCE SAFETY AND SECURITY ACTIVITY D PORADA 23 STRAUSS AVE INDIAN HEAD MD 20640
1	NAVAL ORDNANCE SAFETY AND SECURITY ACTIVITY FARAGUT HALL BLDG D323 K TOMASELLO 23 STRAUSS AVE INDIAN HEAD MD 20640-1541
1	US NAVAL RESEARCH LAB 4555 OVERLOOK AVE SW CODE 6189 R MOWREY WASHINGTON DC 20375-5342
1	US NAVAL RESEARCH LAB CHEMISTRY DIV CODE 6125 J RUSSELL 4555 OVERLOOK AVE SW WASHINGTON DC 20375-5342
1	COMMANDER NAVAL SEA SYSTEMS COMMAND INDIAN HEAD 101 STRAUSS AVE CODE 910A W KOPPES INDIAN HEAD MD 20640-5035
1	COMMANDER NSWC CTR CRANE CODE 4023 BLDG3347 S D'ARCHE 300 HWY 361 CRANE IN 47522-5001
1	NSWC CTR DAHLGREN CODE G22 BLDG 221 R GARRETT 17320 DAHLGREN RD DAHLGREN VA 22448-5100
1	NSWC CTR DAHLGREN CODE G24 S HOCK 17320 DAHLGREN RD DAHLGREN VA 22448-5100
1	NSWC CTR DAHLGREN CODE G24 B KNOTT 17320 DAHLGREN RD DAHLGREN VA 22448-5100
1	NSWC CTR DAHLGREN E LACY 17320 DAHLGREN RD DAHLGREN VA 22448
1	NSWC CTR DAHLGREN CODE G22 S WAGGENER 17320 DAHLGREN RD DAHLGREN VA 22448-5100
1	NSWC INDIAN HEAD CODE 910 W BLDG 600 V BELLITTO 101 STRAUSS AVE INDIAN HEAD MD 20640
1	NSWC INDIAN HEAD BLDG 600 J CAREY 101 STRAUSS AVE INDIAN HEAD MD 20640
1	NSWC INDIAN HEAD CODE 440C P CARPENTER 101 STRAUSS AVE INDIAN HEAD MD 20640
1	NSWC INDIAN HEAD CODE 910F J CHANG 101 STRAUSS AVE INDIAN HEAD MD 20640
1	NSWC INDIAN HEAD D CICHRA 101 STRAUSS AVE INDIAN HEAD MD 20640-5035

NO. OF COPIES ORGANIZATION

1 NSWC
INDIAN HEAD
EXPLOSIVES TEST & DEVELOPMENT
CODE 370
D COOK
101 STRAUSS AVE BLDG 695
INDIAN HEAD MD 20640

1 NSWC
INDIAN HEAD
R CRAMER
101 STRAUSS AVE
INDIAN HEAD MD 20640

1 NSWC
INDIAN HEAD
CODE 90D
R DOHERTY
101 STRAUSS AVE
INDIAN HEAD MD 20640-5035

1 NSWC
INDIAN HEAD
M DUNN
101 STRAUSS AVE BLDG 695
INDIAN HEAD MD 20640-5035

1 NSWC
INDIAN HEAD
CODE ST
A DUONG
101 STRAUSS AVE
INDIAN HEAD MD 20640-5035

1 NSWC
INDIAN HEAD
BLDG 600
F FOROHAR
101 STRAUSS AVE
INDIAN HEAD MD 20640-5035

1 NSWC
INDIAN HEAD
CODE 920J
R GUIRGUIS
101 STRAUSS AVE
INDIAN HEAD MD 20640-5035

1 NSWC
INDIAN HEAD
R JONES
101 STRAUSS AVE
INDIAN HEAD MD 20640

NO. OF COPIES ORGANIZATION

1 NSWC
INDIAN HEAD
RESEARCH & TECHNOLOGY DEPT
CODE 9100 BLDG 600
J HARPER
101 STRAUSS AVE
INDIAN HEAD MD 20640-5035

1 NSWC
INDIAN HEAD
ENERGETIC MATERIALS RESEARCH
CODE 920L BLDG 600
V JOSHI
101 STRAUSS AVE
INDIAN HEAD MD 20640-5035

1 NSWC
INDIAN HEAD
RESEARCH & TECH DEPT
CODE 910R
R JOUET
101 STRAUSS AVE
INDIAN HEAD MD 20640-5035

1 NSWC
INDIAN HEAD
BLDG 490 ROOM 220
C KNOTT
101 STRAUSS AVE
INDIAN HEAD MD 20640

1 NSWC
INDIAN HEAD
BLDG 600
J MANNION
101 STRAUSS AVE
INDIAN HEAD MD 20640

1 NSWC
INDIAN HEAD
BUILDING D 323 CODE 4210M
R MCCALL
101 STRAUSS AVE
INDIAN HEAD MD 20640

1 NSWC
INDIAN HEAD
CODE 90
P MILLER
101 STRAUSS AVE
INDIAN HEAD MD 20640

NO. OF COPIES	ORGANIZATION
1	NSWC INDIAN HEAD CODE 920D BLDG 600 S MILLER 101 STRAUSS AVE INDIAN HEAD MD 20640
1	NSWC INDIAN HEAD CODE 920 G PANGILINAN 101 STRAUSS AVE INDIAN HEAD MD 20640
1	NSWC INDIAN HEAD CODE 920U BLDG 600 L PARKER 101 STRAUSS AVE INDIAN HEAD MD 20640
1	NSWC INDIAN HEAD CODE 920P BLDG 600 S PEIRIS 101 STRAUSS AVE INDIAN HEAD MD 20640
1	NSWC INDIAN HEAD D ROSENBERG 101 STRAUSS AVE INDIAN HEAD MD 20640
1	NSWC INDIAN HEAD CODE 370JG BLDG 695 J ROGERSON 101 STRAUSS AVE INDIAN HEAD MD 20640
1	NSWC INDIAN HEAD J SALAN 101 STRAUSS AVE INDIAN HEAD MD 20640
1	NSWC INDIAN HEAD CODE CSE BLDG 600 A STERN 101 STRAUSS AVE INDIAN HEAD MD 20640-5035

NO. OF COPIES	ORGANIZATION
1	NSWC INDIAN HEAD CODE 4210D C WALSH 101 STRAUSS AVE INDIAN HEAD MD 20640
1	NSWC INDIAN HEAD CODE 910X BLDG 600 A WARREN 101 STRAUSS AVE INDIAN HEAD MD 20640
1	OFFICE OF NAVAL RESEARCH C BEDFORD 800 N QUINCY ST ARLINGTON VA 22217
1	NAVAL AIR SYSTEMS COMMAND PATUXENT (NAVAIR) HQ AIR 4 7 48150 SHAW RD BLDG 2109 RM 122 A GEHRIS PATUXENT RIVER MD 20670
1	OFFICE OF SECRETARY OF DEFENSE ODUSD/S&T 1777 N KENT ST STE 9030 D TAM ARLINGTON VA 22209
1	PENTAGON LW&M LAND WARFARE & MUNITIONS D BAUM OUSD(AT&L)/DS/LW&M RM 3B1060 3090 DEFENSE PENTAGON WASHINGTON DC 20301-3090
1	OUSD(AT&L)/DS/LAND WARFARE & MUNITIONS S ROJAS RM 3B1060 3090 DEFENSE PENTAGON WASHINGTON DC 20301-3090
1	ARGONNE NATIONAL LAB K CARNEY PO BOX 2528 IDAHO FALLS ID 83404

NO. OF COPIES	ORGANIZATION
1	ARGONNE NATL LAB CHEMISTRY DIV J HESSLER 9700 SOUTH CASS AVE ARGONNE IL 60439-4831
1	LAWRENCE LIVERMORE NATL LAB PO BOX 808 L 092 A GASH LIVERMORE CA 94551
1	LAWRENCE LIVERMORE NATL LAB MS L 30 A KUHL PO BOX 808 LIVERMORE CA 94550
1	LAWRENCE LIVERMORE NATL LAB L 282 J MOLITORIS PO BOX 808 LIVERMORE CA 94551
1	LOS ALAMOS NATL LAB MS P918 DX DO W DANEN LOS ALAMOS NM 87545
1	LOS ALAMOS NATL LAB MS E549 K HUBBARD LOS ALAMOS NM 87545
1	LOS ALAMOS NATL LAB MS C920 S SON LOS ALAMOS NM 87545
1	LOS ALAMOS NATL LAB GROUP DX 2 MS C920 B TAPPAN LOS ALAMOS NM 87545
1	SANDIA NATL LAB MS 0836 M BAER ALBUQUERQUE NM 87185-0836
1	SANDIA NATL LAB MS 0836 E HERTEL ALBUQUERQUE NM 87185-0836

NO. OF COPIES	ORGANIZATION
1	SANDIA NATL LAB MS 1172 T HITCHCOCK PO BOX 5800 ALBUQUERQUE NM 87185-1172
1	SANDIA NATL LAB PO BOX 5800 MS 1452 B INGRAM ALBUQUERQUE NM 87185-1452
1	SANDIA NATL LAB PO BOX 5800 MS 1454 M KANESHIGE ALBUQUERQUE NM 87185-1454
1	SANDIA NATL LAB PO BOX 5800 MS 1452 B MELOF ALBUQUERQUE NM 87185-1452
1	SANDIA NATL LAB PO BOX 5800 MS 1454 A RENLUND ALBUQUERQUE NM 87185-1424
1	DEFENSE THREAT REDUCTION AGENCY TDSH J KOLTS 8725 JOHN J KINGMAN RD STOP 6201 FORT BELVOIR VA 22060
1	DCI CTR FOR WEAPONS INTELLIGENCE NONPROLIFERATION & ARMS CONTROL WINPAC M AGUILO WASHINGTON DC 20505
1	J BACKOFEN 2668 PETERSBOROUGH ST HERNDON VA 20171-2443
1	US GOVERNMENT C LLOYD 47110 SOUTHAMPTON STERLING VA 20165

NO. OF COPIES	ORGANIZATION
1	DCI CTR FOR WEAPONS INTELLIGENCE NONPROLIFERATION & ARMS CONTROL WINPAC J WALTON WASHINGTON DC 20505
1	DEFENSE INTELLIGENCE AGENCY BLDG 6000 DWO 4 K CRELLING BOLLING AIR FORCE BASE WASHINGTON DC 20340-5100
1	AEROJET E LIU PO BOX 13222 SACRAMENTO CA 95813
1	ALLIANT TECH SYSTEMS INC C ZISETTE PO BOX 1 RADFORD VA 24141
1	APPLIED RESEARCH ASSOC C NEEDHAM 4300 SAN MATEO BLVD NE SUITE A 220 ALBUQUERQUE NM 87110
1	ARGONIDE CORP F TEPPER 291 POWER CT SANFORD FL 32771
1	ATK THIOKOL PROPULSION PO BOX 707 MS 244 J AKESTER BRIGHAM CITY UT 84302-0707
1	ATK THIOKOL PROPULSION PO BOX 707 M/S 244 P BRAITHWAITE BRIGHAM CITY UT 84302
1	ATK THIOKOL PROPULSION PO BOX 707 MS 230 S GLAITTLI BRIGHAM CITY UT 84302-0707
1	ATK THIOKOL PROPULSION PO BOX 707 MS 244 K LEE BRIGHAM CITY UT 84302-0707
1	ATK THIOKOL PROPULSION PO BOX 707 MS 244 G LUND BRIGHAM CITY UTAH 84302
1	ATK THIOKOL PROPULSION PO BOX 707 MS 230 S LUSK BRIGHAM CITY UT 84302-0707
1	BATTELLE MEMORIAL INSTITUTE T BURKY 505 KING AVE COLUMBUS OH
1	BOOZ ALLEN HAMILTON G ZUCCARELLO 3811 N FAIRFAX DR STE 600 ARLINGTON VA 22203
1	CACI INC M EGGLESTON 14151 PARK MEADOW DR CHANTILLY VA 20151
1	DE TECHNOLOGIES INC C FORSYTH 3620 HORIZON DR KING OF PRUSSIA PA 19406
1	ENERGETIC MATRL APPLICATIONS L JOSEPHSON 300 DAWN CT RIDGECREST CA 93555
1	ENSIGN BICKFORD AEROSPACE & DEFENSE A GARVEY 640 HOPMEADOW ST BLDG 46 SIMSBURY CT 06070
1	EXOTHERM CORP A LASCHIVER 1035 LINE ST CAMDEN NJ 08103
1	GENERAL SCIENCES INC P ZAVITSANOS 205 SCHOOLHOUSE RD SOUDERTON PA 18964

NO. OF COPIES ORGANIZATION

1 GEO CENTERS INC
BLDG 3028
D PARITOSH
PICATINNY ARSENAL NJ 07806-5000

1 HICKS & ASSOC INC
SUITE 1300
C KITCHENS JR
1710 SAIC DR
MCLEAN VA 22102

1 NANOTECHNOLOGIES INC
D HAMILL
1908 KRAMER LN
AUSTIN TX 78758

1 NORTHROP GRUMMAN CORP/DTRA
J COCCHIARO
6940 S KINGS HIGHWAY STE 210
ALEXANDRIA VA 22310

1 NORTHROP GRUMMAN IT
M SEIZEW
PO BOX 471
SAN PEDRO CA 90733-0471

1 PRATT & WHITNEY
N TRIVEDI
600 METCALF RD
SAN JOSE CA 95138

1 ST MARKS POWDER
A GENERAL DYNAMICS CO
J DRUMMOND
PO BOX 222
ST MARKS FL 32355

1 SAIC
W WAESCHE
4319 BANBURY DR
GAINESVILLE VA 20155

1 SRI INTERNATIONAL
J BOTTARO
ROOM PS 318
333 RAVENSWOOD AVE
MENLO PARK CA 94025

1 TALLEY DEFENSE SYS
G KNOWLTON
40512 NORTH HIGLEY RD
MESA AZ 85205

NO. OF COPIES ORGANIZATION

ABERDEEN PROVING GROUND

26 DIR USARL
AMSRD ARL WM B
A HORST
AMSRD ARL WM BD
W ANDERSON
R BEYER
A BRANT
S BUNTE
E BYRD
L CHANG
J COLBURN
P CONROY
B FORCH
B HOMAN
P KASTE
A KOTLAR
C LEVERITT
K MCNESBY
M MCQUAID
A MIZIOLEK
M NUSCA
R PESCE-RODRIGUEZ
B RICE
R SAUSA
AMSRD ARL WM TB
P BAKER
D KOOKER
B KRZEWINSKI
R LOTTERO
B ROOS

INTENTIONALLY LEFT BLANK.